fire

MDPI

Article

Coupled Effects of Wind and Slope on Critical Fire Behaviors of Cables in Inclined Tunnels

Yutao Zhang [1], Linjia Wang [1,*], Rui Liu [2], Yuanbo Zhang [1], Hang Song [1], Qiang Guo [1], Jing Bian [3] and Haochen Li [1]

[1] School of Safety Science and Engineering, Xi'an University of Science and Technology, Xi'an 710054, China
[2] Shaanxi Yulin Energy Group Guojiatan Mining Co., Ltd., Yulin 719000, China
[3] Shennan Industrial Development Co., Ltd. of Shaanxi Coal and Chemical Industry Group, Shenmu 719300, China
* Correspondence: wanglinjia@stu.xust.edu.cn

Abstract

To systematically examine the effects of ambient wind speed on the fire behavior of inclined tunnel cables, this paper determines the combustion characteristics of ZR-RVV cable combustion parameters using synchronous thermal analysis and cone calorimetry. A 1:20 scaled tunnel platform was established based on Froude similarity criterion to conduct combustion experiments under varying wind speeds (0–0.7 m/s) and inclination angles (−30°–30°). Results indicate the ignition time of the cable decreases gradually with increasing external heating radiation intensity (25–50 kW/m^2), with ignition at 295.1 °C. A modified Richardson number (*Ri**) is introduced to quantitatively identify the dominant flow regime. It is confirmed that when $|\theta| \approx 20°$, $Ri^* \approx 1$, and the fire behavior transitions from "domination" ($Ri^* < 0.5$) to "buoyancy-driven stack effect domination" ($Ri^* > 2$). This critical inclination angle provides decisive guidance for fire source localization, smoke control, and exhaust design. Increasing ambient wind speed significantly reduces the fire temperature and dilutes the smoke; at a wind speed of 0.7 m/s, the maximum temperature drop at the ceiling monitoring point reaches 67%, while CO/CO_2 concentrations decrease correspondingly. The findings provide a theoretical basis for smoke exhaust design and fire monitoring in tunnel fire protection.

Keywords: inclined tunnel fire; ambient wind speed; cable fire; combustion characteristics; Richardson number

1. Introduction

With rapid urbanization, tunnels have emerged as vital arteries in modern transportation networks, where integrated cable systems play a pivotal role in enabling high-capacity power transmission infrastructure upgrades [1]. Nevertheless, the confined geometry of tunnels inherently amplifies fire risks, particularly in inclined configurations dictated by geomorphological constraints [2,3]. Such slopes exacerbate fire dynamics through intensified chimney effects, which accelerate flame propagation and toxic smoke dispersion [4–6], as evidenced by catastrophic incidents like the 2014 Yanhou Tunnel fire in China (40 fatalities, 12 injuries). These incidents underscore the imperative to resolve combustion mechanisms of cable fires in sloped tunnels—a critical gap in urban energy infrastructure safety.

A large number of scholars have conducted in-depth research cable pyrolysis and combustion behaviors using cone calorimetry, thermogravimetry and Fourier transform infrared spectroscopy and other means [7–9]. Experimental studies confirm linear correlations between external heat flux and mass loss rates for PVC-insulated cables [10–12].

Check for updates

Academic Editor: Kaihua Lu

Received: 13 May 2026
Revised: 26 June 2026
Accepted: 1 July 2026
Published: 3 July 2026

Copyright: © 2026 by the authors. Licensee MDPI, Basel, Switzerland. This article is an open access article distributed under the terms and conditions of the Creative Commons Attribution (CC BY) license.

Chen et al. [13] found experimentally that flame spread rate (FSR) and mass loss rate (MLR) of cables are positively correlated with bending angles. Peng et al. [14] and Zheng et al. [15] conducted experiments on a single cable and the cable ignition process, respectively, and revealed the critical roles of the cable diameter, the insulating material, and the flame-retardant material in the fire. In tunnel or corridor environments, cable combustion characteristics are more complex: Huang et al. [16] revealed the vertical temperature stratification law in cable fire scenarios through full-size corridor experiments, while Chen et al. [17] observed accelerated flame spread and earlier peak temperature attainment with increasing tunnel inclinations. Also, they explored the combustion characteristics of single-row bridge cables and found that the heat release rate decreases with increasing cable spacing [18]. Xing et al. [19] highlighted the dominance of thermal radiation flux in mobile cable fires within full-scale corridors. In addition, experimental influences such as cable arrangement, cables and bridges, and the location of cables in a duct corridor have been studied by a large number of scholars [20,21]. While Hay et al. [22] used CFD to simulate PVC cable fires in horizontally long cable bridges to explore the flame front spreading mechanism. In terms of the effect of ventilation conditions on cable combustion, the study by Liu et al. [23] revealed the smoke characteristics of cable fires in L-type integrated duct corridors under different ventilation conditions, pointing out the importance of the location of the air inlet in slowing down the fire temperature and decreasing the rate of CO diffusion, while Zhu et al. [24] used simulation to quantitatively assess the risk of cable fires in integrated duct corridors. Many scholars have also used CFD and FDS modeling, experimental validation, and natural ventilation conditions to thoroughly investigate the effects of ventilation flow rate, air inlet location, and natural ventilation on the heat release rate and thermal properties of cable fires [25–27].

In summary, although existing studies have thoroughly investigated the combustion characteristics of cables themselves and their behavior under specific ventilation or inclined conditions, most have treated wind speed and inclination angle as independent variables. For the typical scenario of an inclined tunnel, there exists a strong coupling effect between ambient wind speed and tunnel inclination. At present, how this coupling effect quantitatively influences flame morphology, temperature, and smoke production, as well as the underlying physical mechanisms and critical conditions for the transition of dominant modes, remains to be revealed. Therefore, this study aims to systematically investigate the coupled influence mechanism of ambient wind speed and tunnel inclination on cable fire spread characteristics through scaled model experiments, starting from the fundamental principle of buoyancy–inertia competition. The goal is to identify key control parameters and critical conditions, thereby providing a more precise theoretical basis for active fire prevention and control in tunnel fires.

2. Experimental Materials and Methods

2.1. Experimental Materials

In this study, the flame-retardant 0.6/1 kV copper-core polyvinyl chloride (PVC) insulated and sheathed flexible power cable, designated as ZR-RVV cable (hereinafter referred to as “cable”), is selected as the research object. The ZR-RVV cable used in this study was supplied by Henan Pacific Cable Co., Ltd., Jiaozuo, China. Cable samples are prepared in accordance with the experimental standard requirements, with dimensions of 100 mm × 100 mm and a cable thickness of 10 mm. The cable is directly cut into 100 mm lengths and arranged transversely to a width of 10 mm for the experiment.

The combustion characteristics of cable materials serve as important parameters for evaluating their fire hazard. Accordingly, a cone calorimeter (FTT CONE, Kunshan Mottis, Suzhou, China) is employed to investigate the ignition time and heat release rate (HRR)

of the cable. Ignition time is a key parameter characterizing the pyrolysis behavior and fire hazard of a material; a shorter ignition time indicates that the material is more easily ignited and poses a greater fire risk [10]. The heat release rate directly reflects the average combustion energy released by the cable [28]. In addition, the experimental external heating radiation intensity were: 25, 30, 35, 40, 45, and 50 kW/m^2, corresponding to the level of thermal radiation of small-scale fires and medium-scale fires in the tunnel. Thermal radiation module: Comprising a radiant heating plate and a temperature control cabinet with a heating range of 0~500 °C [29].

2.2. Small-Scale Experimental Model and Test Conditions

2.2.1. Similarity Model Theory and Construction

In the construction of the fire model, the Froude similarity criterion is typically applied to ensure a fixed scaling ratio between the parameters of the model tunnel (m) and the prototype tunnel (f). This requires maintaining a constant Froude number $Fr = v\sqrt{gl}$. The Froude number represents the ratio between inertial and buoyancy/gravity effects, and it is commonly used in reduced-scale tunnel fire experiments where plume motion and smoke transport are mainly governed by buoyancy–inertia interaction. Although Reynolds number similarity cannot be simultaneously satisfied in such reduced-scale fire models, Froude scaling has been widely adopted in 1:20 scale tunnel fire studies with longitudinal ventilation [30,31].

$$\lambda_l = \frac{l_m}{l_f} \tag{1}$$

$$\lambda_A = \frac{A_m}{A_f} = \frac{l_m^2}{l_f^2} = \lambda_l^2 \tag{2}$$

$$\lambda_v = \frac{v_m}{v_f} = \frac{l_m^3}{l_f^3} = \lambda_l^3 \tag{3}$$

where λ_l is the length scale ratio; l_m is the length of the scaled-down model, m; l_f is the Length of the prototype tunnel, m; λ_A is the area scale ratio; A_m is the area of the scaled-down model, m^2; A_f is the area of the prototype tunnel, m^2; λ_v is the volume scale ratio; v_m is the volume of the scaled-down model, m^3; v_f is the volume of the prototype tunnel, m^3.

Kinematic similarity encompasses the similarity of velocity and acceleration. The proportional relationships for velocity similarity and acceleration similarity are expressed as follows:

$$\lambda_u = \frac{u_m}{u_f} = \frac{l_m/t_m}{l_f/t_f} = \frac{\lambda_l}{\lambda_t} \tag{4}$$

$$\lambda_a = \frac{a_m}{a_f} = \frac{l_m/t_m^2}{l_f/t_f^2} = \frac{\lambda_l}{\lambda_t^2} \tag{5}$$

where λ_u is the velocity scale ratio; u_m is the velocity in the scaled-down experiment model, m/s; u_f is the velocity of the prototype tunnel, m/s; t_m is the time in the scaled-down experiment model, s; t_f is the time of the prototype tunnel, s; λ_t is the time scale ratio; λ_a is the acceleration scale ratio; a_m is the acceleration in the scaled-down experiment model, m/s^2; a_f is the acceleration of the prototype tunnel, m/s^2.

Based on the typical cross-sectional dimensions of a full-scale tunnel (width: 12 m, height: 9 m), a 1:20 scale experimental platform was constructed. The scaled-down tunnel features an arched shape, with the main body dimensions of length × width × height is 10 m × 0.6 m × 0.4 m. The cable combustion frame measures length × width × height: 60 cm × 25 cm × 25 cm. The tunnel main body adopts a segmented structure. Both ends

of the vault centerline are made of stainless steel and crystallized glass (glass-ceramic), respectively, to better meet the experimental requirements.

The stainless steel arch on one side facilitates the installation of temperature and smoke sensors, while the crystallized glass on the other side has high heat resistance and is used for observing and recording experimental data during the test. Schematic and internal views of the experimental platform are shown in Figures 1 and 2. The cable is ignited using an external butane igniter, with a maximum temperature of up to 1000 °C. The igniter is placed directly beneath the cable and is removed after the cable reaches stable combustion.

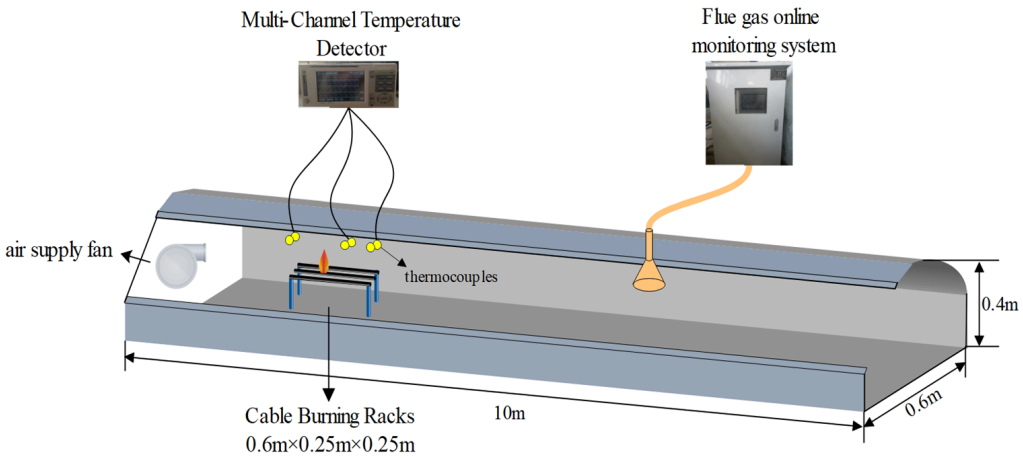


Figure 1. Simplified diagram of the experimental platform.



Figure 2. Internal diagram of the experimental platform.

2.2.2. Experimental Test Conditions

Smoke and temperature are the most critical parameters reflecting the scale and hazards of tunnel fires. Therefore, this study focuses on the temperature distribution in the fire near-field zone and the total smoke evolution during cable combustion in the tunnel. Referring to the commonly used cable cross-sectional area of 30 mm^2, and according to the geometric similarity Equations (1) and (2), a test cable with a length of 60 cm and a cross-sectional area of 1.5 mm^2 is selected for the experiment. To ensure experimental repeatability, each test condition was repeated three times under the same operating parameters. The results reported in this study are the averaged values of the repeated measurements.

Temperature monitoring

K-type sheathed thermocouples with a measurement range of 0 °C to 800 °C are used as temperature sensors. The temperature recorder is a 32-channel data logger (model:

Huipu TCP-XL), with a temperature measurement range of −200~1300 °C, a recording speed of once per 0.1 s, and a measurement accuracy of ±0.2%. Based on the temperature fluctuation time observed in preliminary experiments, and since the present study does not require a particularly high sampling rate, the sampling interval is set to record data once every 5 s.

Smoke monitoring

The smoke monitoring subsystem (Honeyeagle, Shenzhen, China) incorporates CO and CO_2 concentration sensors, with a sampling flow rate of 3~5 L/min. The CO measurement range is 0~5000 ppm with an accuracy of ±2%; the CO_2 measurement range is 0~10% Vol with an accuracy of ±2%. Due to the slow variation in smoke flow, no high-frequency sampling was required. The sampling rate for the smoke system was set to record data every 10 s. The system's storage temperature range is −40 to 70 °C. To adapt to the experimental environment, the online monitoring system was positioned 4.5 m away from the fire source.

Wind speed control

The wind speed regulation subsystem consists of a fan (model: CYUF-315, 50 Hz, 220 V, maximum power: 215 W) and a control valve, as shown in Figure 3. Wind speed was measured using a HT9829 thermal anemometer with a range of 0.1~25 m/s and a resolution of 0.01 m/s.



Figure 3. Wind speed control system.

According to the Chinese standard Guidelines for Ventilation Design of Highway Tunnels [32], the ventilation speed during normal tunnel operation is 2~3 m/s. In the present study, however, the experimental wind speed was determined according to the Froude similarity criterion for a 1:20 reduced-scale tunnel model. Based on the similarity criterion (Equation (4)), the corresponding model-scale velocity range is approximately 0.45~0.67 m/s. Therefore, the selected wind velocities of 0.5, 0.6, and 0.7 m/s reasonably represent the typical ventilation conditions of the prototype tunnel.

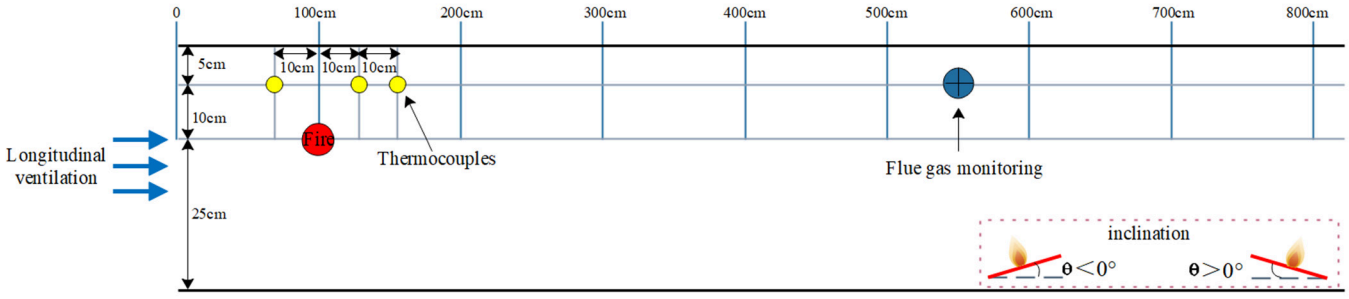
Flame Spread Detection Subsystem

The flame spread detection subsystem consists of a high-speed camera and image processing technology. The high-speed camera model is AZ9501, with a maximum resolution of 1280 × 1024, a maximum frame rate of 2420 FPS, a sensor sensitivity of Mono ISO 400~6400, and an output image file format of MP4 or MPEG. Image processing is performed using MATLAB software (version 5.6). The collected flame videos are decomposed into frames through image processing codes, followed by grayscale processing. Then, an appropriate threshold is set to binarize the images, enabling the calculation of

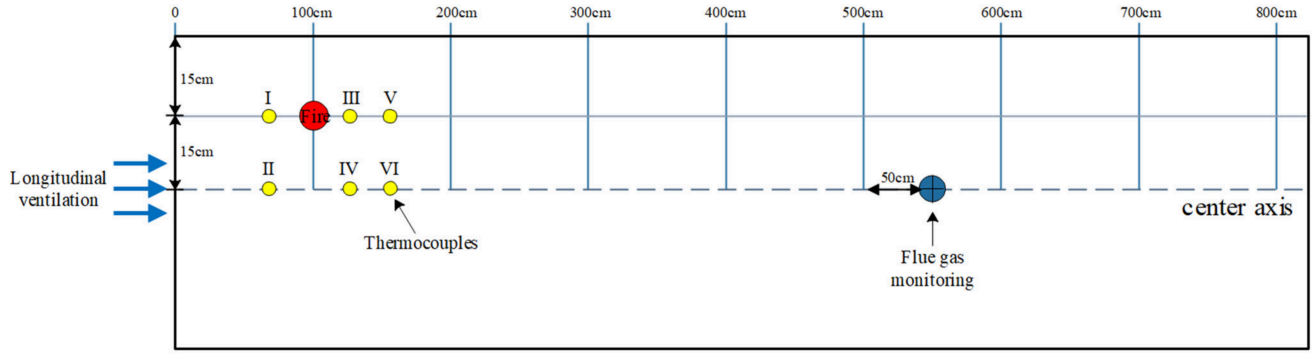
flame height and flame width. The flame spread rate is further derived based on the scaling ratio between image pixels and actual dimensions.

Measurement point layout

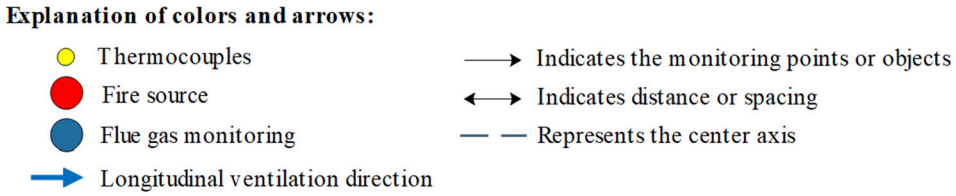
The layout of temperature and smoke measurement points is shown in Figure 4. Within the experimental system: A cable combustion frame was installed 15 cm from the tunnel's central axis. Six thermocouple measurement points (Points I~VI) were arranged around the fire source, vertically 5 cm below the tunnel vault. Points I, III, and V were linearly aligned directly above the cable along the tunnel's longitudinal direction, 15 cm horizontally from the central axis. Points adjacent to the fire center were positioned 10 cm from the fire center, with an additional point placed 10 cm downstream. Points II, IV, and VI were symmetrically arranged above the central axis. Previous studies indicate that parameters stabilize when the measurement length reaches 10 times the diameter. Given the scaled-down tunnel's height of 0.4 m, smoke concentration measurement points were placed 5 cm below the vault along the central axis and 4.5 m from the fire center.



(**a**) Main view



(**b**) Vertical view



(**c**) Explanation of colors and arrows

Figure 4. Layout of measurement points in the scaled-down experiment.

In accordance with the Chinese standard Guidelines for Lighting Design of Highway Tunnels [33], the maximum gradient of urban roads is generally 40%. Since cables are typically laid parallel to the tunnel floor, the experiment simulated cable inclinations matching the tunnel slope. Cable tilt angles were set to −30°, −20°, −10°, 0°, 10°, 20°, and 30°, with negative angles defined as tilting toward the fan.

3. Results and Discussion

3.1. Hazard Characteristics of Cable Combustion

(1) Ignition Time

Ignition time is defined as the interval from the moment the external radiant heat flux is first applied to the cable sample to the moment when a sustained flame appears on the cable surface and continues for 10 s. Table 1 shows the ignition time of cables under different external radiant heat flux levels. The results indicate that as the radiant heat flux increases, the ignition time of the cable decreases significantly. This occurs because higher radiant heat flux elevates the cable's surface temperature, accelerating its pyrolysis process and releasing more combustible volatile gases from the surface, thereby shortening the ignition time. Specifically: At a radiant heat flux of 25 kW/m^2, the ignition time is 450 s. When the radiant heat flux increases to 50 kW/m^2, the ignition time drops sharply to 16 s. These findings demonstrate that higher radiant heat flux increases the likelihood of cable ignition, corresponding to an elevated fire risk. The nomenclature of the symbols used in the mathematical formulations is summarized in Table 2.

Table 1. Ignition time of cables under different radiant heat flux levels.

Radiant Heat Flux (Kw/m^2)	**25**	**30**	**35**	**40**	**45**	**50**
Ignition time (s)	450	217	68	37	32	16

Table 2. Nomenclature used in the mathematical formulations.

Symbol	**Definition**	**Unit**
Fr	Froude number	-
T_{TTI}	Ignition temperature of the material	K
L_0	Thickness of the material	m
ρ	Material density	kg/m^3
C	Specific heat capacity of the material	kJ/(kg·K)
q''_e	External radiant heat flux	kW/m^2
q''_{er}	Critical radiant heat flux	kW/m^2
h_c	Convective heat transfer coefficient	W/K·m^2
ε	Emissivity	-
σ	Constant	W/m^2·K^4
θ_f	Flame tilt angle	°
u	Ambient wind speed	m/s
u_b	Characteristic buoyancy velocity	m/s
Q	Heat release rate	kW
g	Gravitational acceleration	m/s^2
k	Empirical flame-tilt coefficient	-
ρ_∞	Density of ambient air	kg/m^3
c_p	Specific heat capacity at constant pressure	kJ/(kg·K)
T_∞	Ambient absolute temperature	K
Ri	Richardson number	-
Ri^*	Modified Richardson number	-
L	Characteristic length	m

To analyze fire risks in depth, the ignition formula for heat-neutral materials proposed by Xu et al. [34] was introduced, and the model equation is shown in Equation (6).

$$T_{TTI}^{-2/3} \cdot L_0^{1/3} = \frac{(0.65\rho c\sqrt{k})^{-2/3}}{T_{TTI} - T_\infty} \cdot (q_e'' - q_{er}'') \tag{6}$$

where T_{TTI} is the ignition temperature of the material, K; L_0 is thickness of the material, m; ρ is Material density, kg/m^3; c is specific heat capacity of the material, J/(kg·K); k is thermal conductivity of the material, W/(m·K); T_∞ is ambient temperature, K; q_e'' is external radiant heat flux, kW/m^2; q_{er}'' is critical radiant heat flux, kW/m^2.

Equation (7) defines the critical radiant heat flux:

$$q_{er}'' = h_c(T_{TTI} - T_\infty) + \varepsilon\sigma(T_{TTI}^4 - T_\infty^4) \tag{7}$$

where h_c is convective heat transfer coefficient, W/K·m^2, h_c = 10 W/K·m^2; ε is emissivity, $\varepsilon = 1$; σ is constant, W/m^2·K^4, $\sigma = 5.67 \times 10^{-8}$ W/m^2·K^4.

To quantitatively characterize the ignition characteristics of the ZR-RVV cable and obtain its key thermophysical parameters, $T_{TTI}^{-2/3} \cdot L_0^{1/3}$ is plotted against q_e''. As shown in Figure 5, $T_{TTI}^{-2/3} \cdot L_0^{1/3}$ exhibits a linear relationship with q_e''. The slope of the fitted line yields the combined thermophysical parameter of the cable, while the intercept gives the critical radiant heat flux, i.e., q_{er}'' = 0.2857 kW/m^2, with a goodness of fit R^2 = 0.955. Substituting the obtained parameters into Equation (6), the ignition temperature of the cable is determined to be 295.1 °C. The above parameters serve as core indicators for assessing the fire hazard of the cable and also provide input basis for the subsequent flame tilt angle model and numerical simulations.

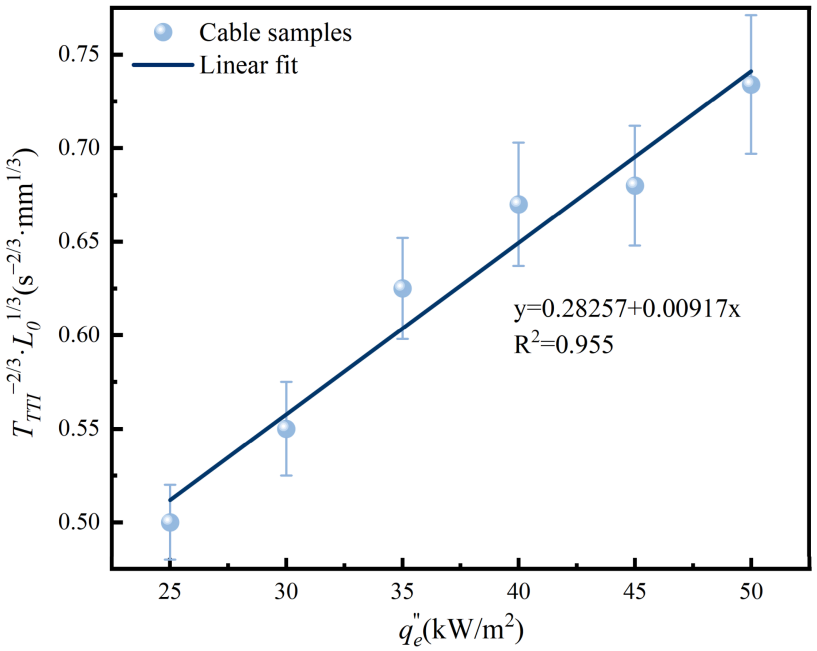


Figure 5. Linear fitting of $T_{TTI}^{-2/3} \cdot L_0^{1/3}$ and q_e''.

To quantitatively characterize the ignition characteristics of the ZR-RVV cable and obtain its key thermophysical parameters, $T_{TTI}^{-2/3} \cdot L_0^{1/3}$ was plotted against q_e''. As shown in Figure 5, the data exhibit an approximately linear trend within the tested radiant heat flux range. The slope of the fitted line was used to estimate the combined thermophysical parameter of the cable, while the intercept was used to derive the critical radiant heat flux, i.e., q_{er}'' = 0.2857 kW/m^2. The obtained fitting result (R^2 = 0.955) indicates that the

linear approximation reasonably describes the relationship within the present dataset. Substituting the obtained parameters into Equation (6), the ignition temperature of the cable was estimated to be 295.1 °C. The error bars in Figure 5 represent one standard deviation from repeated measurements, reflecting the experimental uncertainty of the fitted data. Most data points remain close to the fitted line within the uncertainty range, further supporting the applicability of the linear approximation under the tested radiant heat flux conditions. These parameters provide useful input for evaluating the fire hazard of the cable and for subsequent analysis of flame deflection and thermal behavior.

(2) Heat release rate

Figure 6 shows the heat release rate (HRR) curves of the cable under different radiant heat flux levels over time. The results reveal that the HRR trends are broadly similar across all tested heat flux conditions: The HRR rapidly rises to an initial peak (up to approximately 120 kW/m^2), followed by a slight decline. Subsequently, the rate accelerates again, forming two additional peaks before gradually decreasing until the cable combustion ends. The three distinct HRR peaks correspond to the three-stage pyrolysis combustion process of the cable under external radiant heat. First, the outer sheath material decomposes under radiant heating, releasing combustible volatile gases that ignite. Second, as heat penetrates deeper, the insulation layer and inner sheath generate additional volatiles that combust. Finally, the residual char remaining after gas-phase pyrolysis undergoes further oxidation.

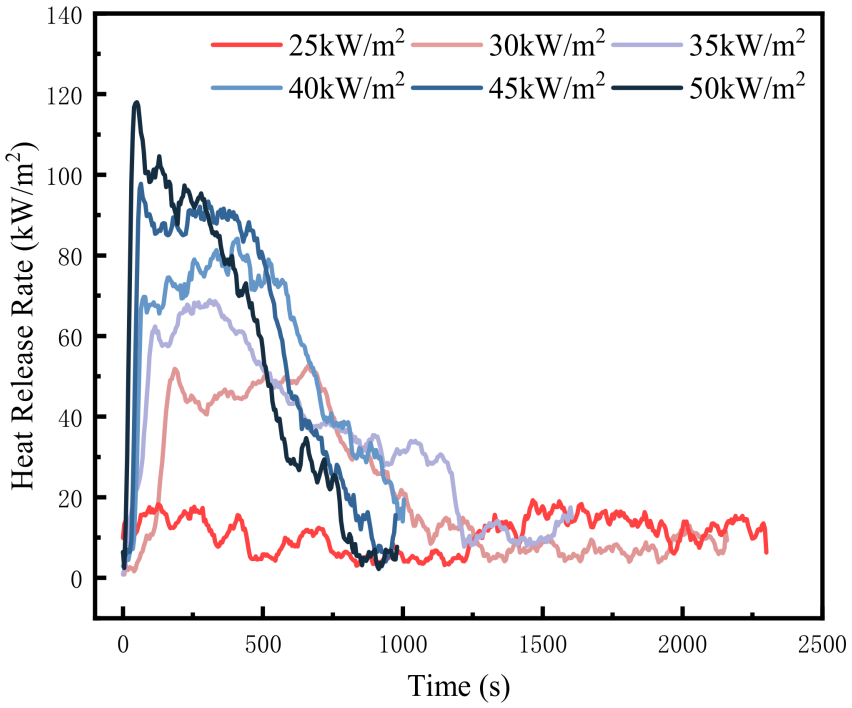


Figure 6. Temporal variation in heat release rate (HRR) of the cable under different radiant heat flux levels.

Moreover, the maximum HRR peak increases with higher external radiant heat flux, and the time required to reach the peak shortens significantly. For instance, under a heat flux of 25 kW/m^2, the HRR stabilizes around 20 kW/m^2 after the initial peak. As the heat flux increases, both the peak occurrence and the decay phase advance, reflecting intensified combustion with reduced total duration. This demonstrates that higher radiant heat flux accelerates the pyrolysis process, shortening the combustion time while increasing the heat released per unit time. Consequently, the HRR peak amplifies, and its timing shifts earlier.

Figure 7 displays the correlation curve between the external radiant heat flux and the maximum HRR peak. Within the tested range, the maximum HRR peak increases approximately linearly with increasing external radiant heat flux, with a fitted R^2 value of 0.968. This fitting result is used to describe the observed experimental trend rather than to establish a universal predictive correlation. The error bars represent the experimental uncertainty of the measurements, and the data points generally remain close to the fitted line within the uncertainty range, indicating good repeatability and consistency of the experimental results. Physically, higher radiant heat flux enhances cable pyrolysis and promotes the release of combustible volatiles, thereby increasing the HRR peak and fire intensity. Therefore, external radiant heat flux plays an important role in intensifying cable combustion and increasing fire risk under the present experimental conditions.

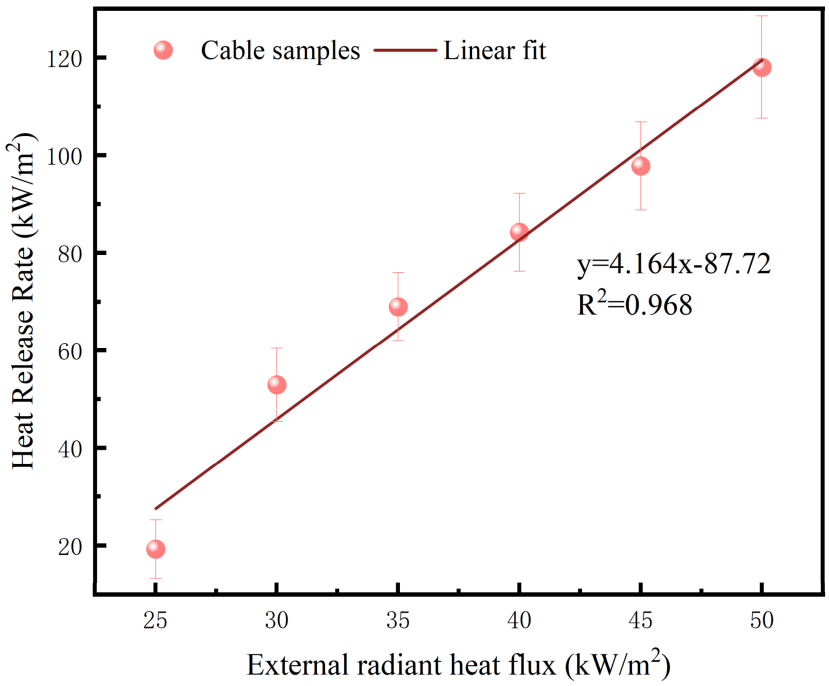


Figure 7. Correlation between external radiant heat flux and maximum HRR peak of the cable.

This section utilizes cone calorimeter experiments to determine the fundamental combustion characteristics of ZR-RVV cable materials. These parameters form the physical basis for understanding their complex behavior in real-world tunnel fire scenarios. These material-level characteristics, particularly the dynamic evolution of heat release rate (HRR), directly determine the intensity and duration of energy release from cables as fire sources. Consequently, they provide critical input parameters for analyzing flame dynamics, temperature field distribution, and smoke generation behavior in inclined tunnels and windy environments. The cable's high thermal release potential indicates its capacity to generate stronger buoyant plumes during fires. The buoyancy intensity is one of the core factors competing with external wind forces, determining flame morphology and propagation trends.

3.2. Influence of Wind Speed on Flame Spread

Based on the aforementioned combustion characteristics of the cable itself, this section further investigates, within a scaled-down tunnel test rig, how two key external conditions—ambient wind speed and tunnel inclination angle—interact with buoyant plume flow to jointly regulate the flame propagation behavior of cable fires.

3.2.1. Patterns of Flame

The average image of the cable during the continuous combustion stage (10 s) is selected. The flame contour is delineated using MATLAB software (version 5.6), and the flame centerline is extracted. The angle between the flame centerline and the normal to the fuel surface is calculated and defined as the flame inclination angle. Figures 8 and 9 depict the flame morphology evolution of cables under windless and windy conditions, respectively.

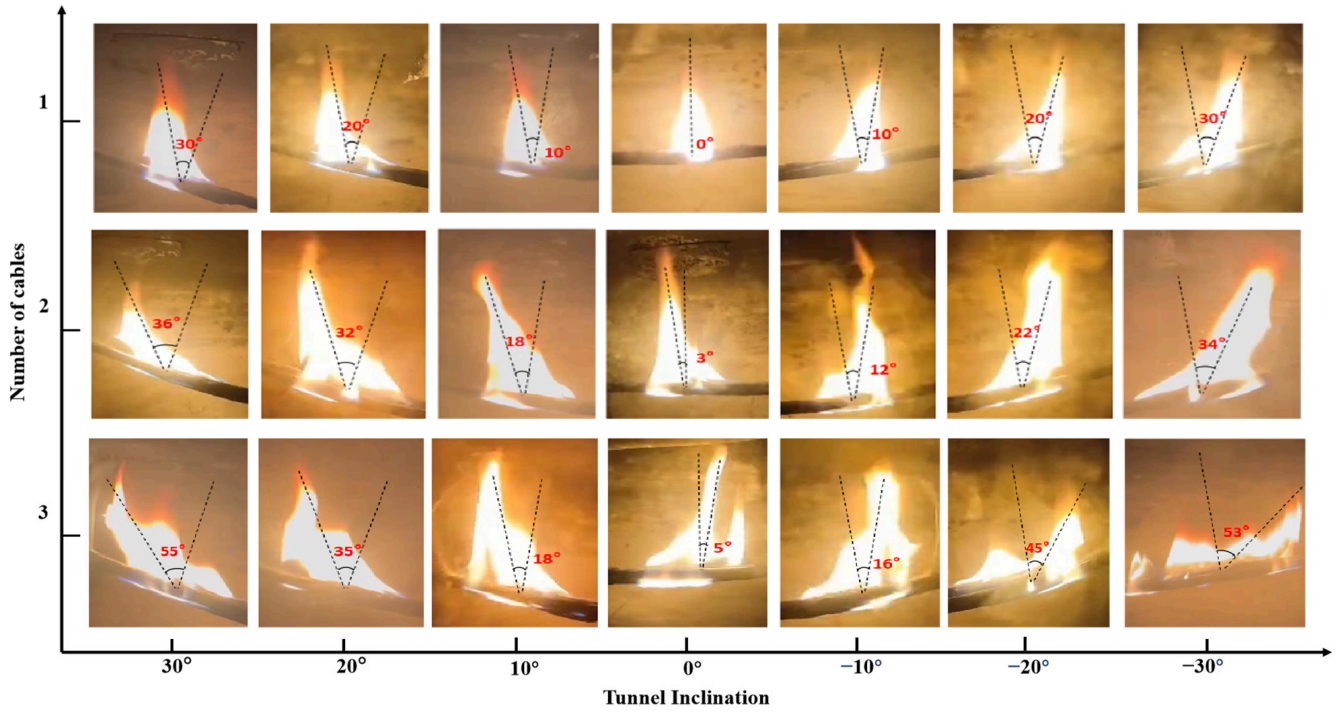


Figure 8. Flame morphology variation in cable combustion under windless conditions.

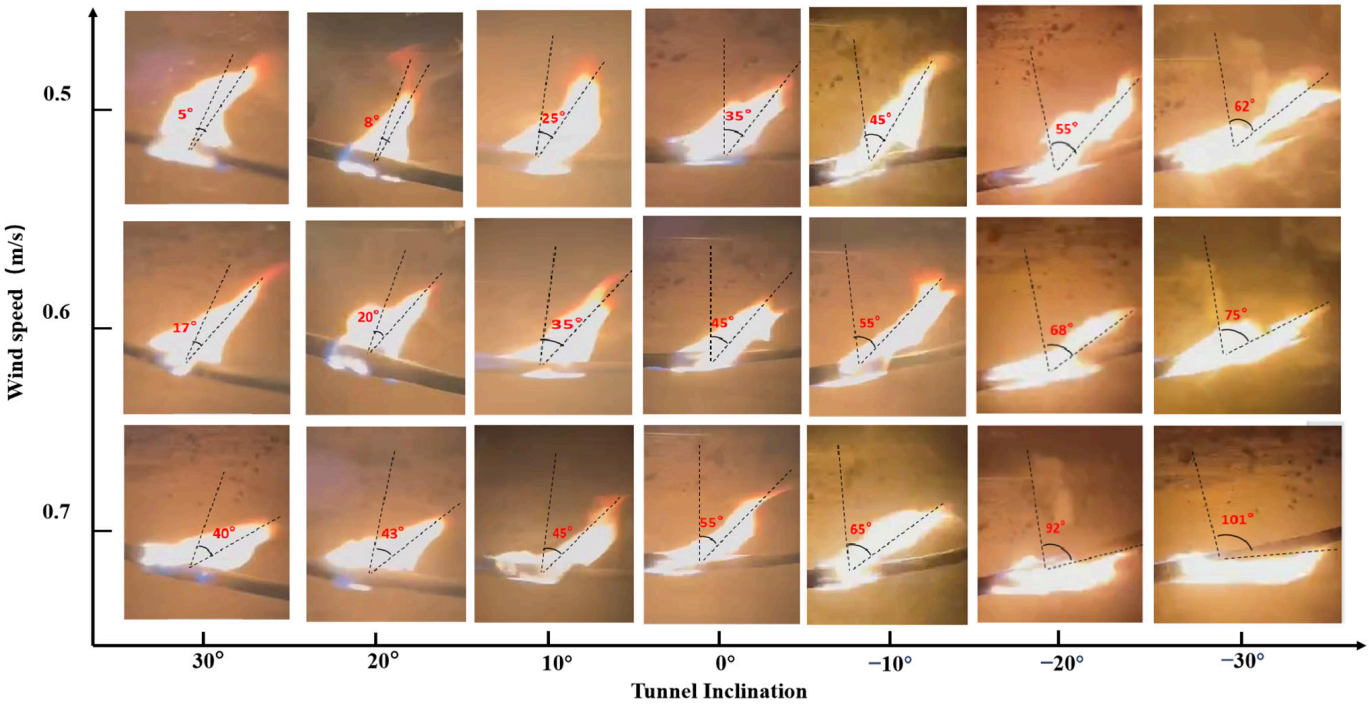


Figure 9. Flame morphology variation in Cable Combustion under windy conditions.

As shown in Figure 8, in the absence of wind, the flame inclination with the increase in the cable inclination angle shows a first decrease and then increase in the law, and the flame inclination and the cable inclination angle changes are basically the same. For a single cable with a 0° tilt angle, the flame displays an axisymmetric shape. As the cable tilt angle changes (0°, 10°, 20°, 30°), the corresponding flame tilt angles align with the cable inclination. This phenomenon arises because the flame tilt angle is defined as the angle between the flame plume centerline and the direction perpendicular to the cable. When the cable tilt angle changes, the perpendicular direction shifts, altering the angle relative to the flame plume centerline. And, the angle of increase and decrease and cable line inclination is closely related to the cable line inclination of the absolute value of the cable line inclination into a positive correlation.

For multiple cables, the general trend of flame tilt angle variation remains consistent with that of a single cable, but the flame tilt angle no longer matches the cable inclination. For example, with three cables burning, the flame tilt angles increase to 5°, 18°, 35°, and 55° as the cable tilt angle rises. This discrepancy is attributed to gaps between cables, which modify flame entrainment patterns and alter the balance between thermal buoyancy and inertial forces. Additionally, as the absolute cable tilt angle increases, the combustion zone expands, leading to a wider flame. Consequently, the angle between the flame centerline and the cable's perpendicular direction becomes larger, resulting in a greater flame tilt angle compared to that of a single cable.

As shown in Figure 9, when ambient wind is present, the flame inclination angle increases significantly with increasing wind speed, and the flame propagation speed also accelerates accordingly. Taking the tunnel inclination angle of −30° as an example, at wind speeds of 0.5 m/s, 0.6 m/s, and 0.7 m/s, the measured flame inclination angles were 62°, 75°, and 101°, respectively.

To quantitatively elucidate the underlying mechanical mechanism of this phenomenon, a flame tilt angle model based on force equilibrium is introduced. The flame tilt angle θ_f is primarily governed by the vertical buoyancy force and the horizontal wind inertia force, with the direction of their resultant force determining the inclination of the flame's principal axis. Based on the principle of force synthesis, the tangent of the flame tilt angle can be approximated as the ratio of horizontal to vertical forces (Equation (8)). Through dimensional analysis and consolidation of constants, this simplifies to the core relationship: the flame tilt angle primarily depends on the ratio of wind speed u to characteristic buoyancy velocity u_b (Equation (9)):

$$\tan\theta_f \approx \frac{Horizontal\ inertial\ force}{Vertical\ buoyancy} \propto \frac{Inertial\ force\ term}{Buoyancy\ term} \tag{8}$$

$$\tan\theta_f = k\frac{u}{u_b} \tag{9}$$

In Equation (9), k is the combined thermophysical constant, which characterizes the comprehensive influence of flame morphology, turbulent mixing characteristics, and fuel surface geometry on flame tilting behavior. For many pool fire and calibration fire experiments, its value generally ranges between 1 and 2, with an empirical value of $k \approx 1.5$ commonly used in standard experiments such as pool fires [35].

$$u_b = \left(\frac{gQ}{\rho_\infty c_p T_\infty}\right)^{1/3} \tag{10}$$

u_b represents the characteristic buoyancy velocity (as shown in Equation (10)), characterizing the intensity of buoyancy-driven flow and correlating with the heat release rate Q of the fire source. Here, ρ_∞, c_p, and T_∞ denote the density of ambient air, specific heat

capacity at constant pressure, and absolute temperature, respectively, which can be considered constant under experimental conditions. The core predictive function of this model is that, given the ambient wind speed u and the heat release rate Q of the cable, the flame inclination angle θ_f can be calculated, thereby quantitatively assessing the location and range of the thermal impact of the flame on the tunnel ceiling. This predictive model can provide a theoretical basis for the layout of fire detectors and the structural fire protection design in inclined tunnels. The main assumptions adopted in the model are summarized in Table 3.

Table 3. Main assumptions of the flame inclination model.

Assumption	Description
Quasi-steady flame	The model describes the time-averaged flame morphology during the stable combustion stage rather than instantaneous flame fluctuations.
Dominant force balance	Flame deflection is mainly governed by wind-induced inertia and thermal buoyancy.
Uniform longitudinal flow	The longitudinal wind speed near the fire source is represented by the measured inlet velocity.
Empirical coefficient	The coefficient k accounts for unresolved effects, including flame pulsation, turbulent mixing, fuel arrangement, and radiative heat feedback.
Engineering application	The model is used to interpret the dominant flame-deflection trend rather than to predict instantaneous flame shape.

A sensitivity analysis was conducted to evaluate the influence of the empirical coefficient k on the predicted flame inclination angle. As shown in Figure 10, increasing k from 1.0 to 2.0 leads to a larger predicted flame inclination angle under all tested wind speeds. However, the monotonic increasing trend with wind speed remains unchanged, indicating that k mainly affects the magnitude of the predicted values rather than the governing physical trend. The experimental data with error bars are closest to the prediction curve obtained with k = 1.5, indicating that k = 1.5 has good applicability to the present cable fire configuration. Therefore, k = 1.5 was adopted in the following analysis.

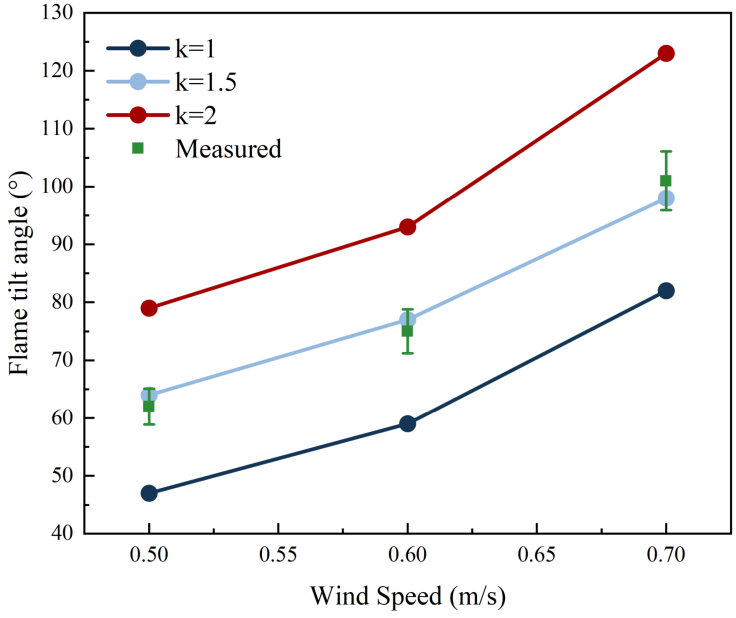


Figure 10. Sensitivity analysis of empirical coefficient k.

The simplified model is mainly used to describe the dominant competition between buoyancy and wind-induced inertia in inclined tunnel cable fires. Within the tested range of longitudinal wind speeds (0–0.7 m/s) and tunnel inclination angles (−30° to 30°), the model can reasonably describe the variation trend of the average flame inclination angle during the stable combustion stage. Since the empirical coefficient k and heat release characteristics may vary with cable type, tunnel geometry, and fire scale, further calibration is recommended when the model is applied to other cable materials or full-scale tunnel scenarios. Nevertheless, the model can reflect the dominant physical mechanism and provide an engineering basis for the preliminary assessment of flame deflection and thermal impact regions in inclined tunnels.

To quantitatively validate the proposed flame inclination model, all measured flame inclination angles under windy conditions were compared with the corresponding predicted values calculated using Equation (9) with k = 1.5. As shown in Figure 11, most data points are distributed close to the 1:1 reference line and fall within the ±5° deviation band, indicating that the simplified model can reasonably predict the average flame inclination angle within the tested range. The statistical indicators further confirm the model performance, with RMSE = 2.38°, MAE = 2.33°, MRE = 2.95%, and R^2 = 0.978. These results suggest that the proposed model captures the dominant buoyancy–inertia competition governing flame deflection, although further calibration is still required for other cable materials, tunnel geometries, and full-scale fire scenarios.

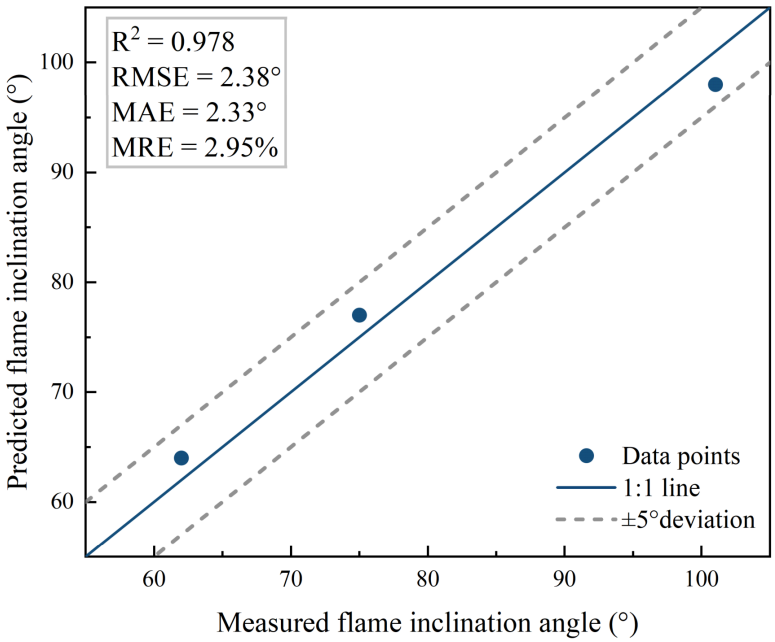


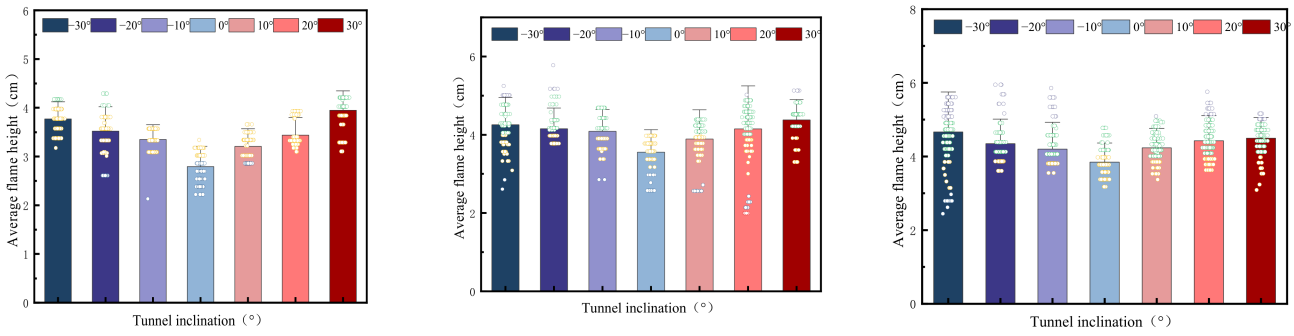
Figure 11. Comparison between measured and predicted flame inclination angles.

Although the experiments were conducted at a reduced scale, previous tunnel fire studies have shown that flame tilt behavior governed by the competition between inertial and buoyancy forces exhibits good similarity across different geometric scales, provided that key dimensionless parameters such as the Froude number or Richardson-type number are preserved. Furthermore, the predicted monotonic increase in flame inclination angle with longitudinal wind speed is consistent with recent experimental studies on tunnel fires under longitudinal ventilation. Chen et al. [36] and Qiu et al. [37] reported similar trends, showing that flame inclination increases with ventilation velocity due to enhanced streamwise inertial forcing and stronger flame deflection. These observations are consistent with the physical mechanism underlying the present buoyancy–inertia based model.

Nevertheless, because the empirical coefficient k and heat-release characteristics may vary with cable type, tunnel geometry, and fire scale, further calibration is recommended when the model is extended to other cable materials or full-scale tunnel scenarios. The model was calibrated using the present experimental dataset, and its applicability is limited to similar ventilation and cable configurations.

3.2.2. Average Flame Height

Figures 12 and 13 present the average flame heights during cable combustion under windless and windy conditions, respectively. As shown in Figure 12, the average flame height initially decreases and then increases with the rise in the cable tilt angle. The minimum flame height occurs at a 0° tilt angle, while larger flame heights are observed at tilt angles of −30° and 30°. Additionally, the average flame height increases with the number of cables. For example: At 0° tilt angle: The average flame heights for single, double, and triple cables are 2.8, 3.5 and 3.82 cm, respectively; At −30° tilt angle: The corresponding heights are 3.75, 4.25, and 4.6 cm; At 30° tilt angle: The heights measure 3.9, 4.3 and 4.5 cm. The non-monotonic variation in flame height with tilt angle arises from the competition between enhanced air entrainment and reduced heat feedback at extreme angles, while the increase in flame height with cable number is driven by cumulative thermal interactions and oxygen depletion effects in multi-cable configurations.



(**a**) 1 cable (**b**) 2 cables (**c**) 3 cables

Figure 12. Average flame height in cable combustion under windless conditions.

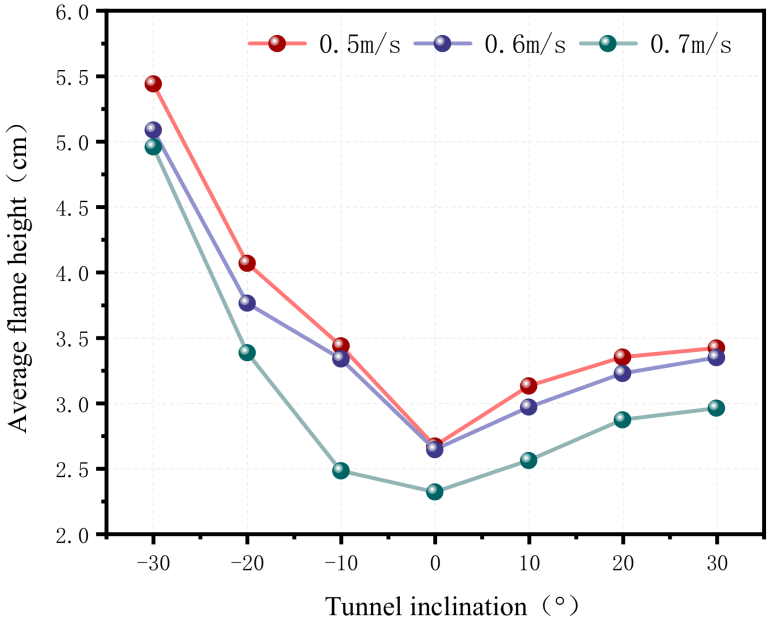


Figure 13. Average flame height in cable combustion under windy conditions.

As shown in Figure 13, when the cable tilt angle is fixed, the average flame height gradually decreases with increasing ambient wind speed. For example, at a 0° tilt angle, under ambient wind speeds of 0.5, 0.6 and 0.7 m/s, the average flame heights measure 2.67, 2.64, and 2.31 cm, respectively. This is attributed to the high-speed airflow elongating the flame structure, shortening flame residence time, and intensifying turbulent mixing at the flame front, which promotes lateral flame expansion over vertical development, thereby reducing the vertical average height.

Additionally, at a constant wind speed, the average flame height increases with larger tilt angles. For instance, at a 0.5 m/s wind speed, as the cable tilt angle increases from 0° to 30°, the average flame heights rise sequentially to 2.67, 3.1, 3.35 and 3.42 cm. This occurs because a larger tilt angle enhances flame adhesion to the cable surface, reducing airflow-induced flame stripping and maintaining higher flame stability.

Notably, under negative tilt angles, flames adhere closer to the cable surface, amplifying radiative heat feedback and accelerating fuel volatilization, which supplies sufficient combustible gases for sustained combustion. In contrast, under positive tilt angles, counteracting winds carry heat away from the fuel surface, weakening heat feedback and slowing volatilization, thereby indirectly limiting flame height. Consequently, average flame heights under negative tilt angles are generally higher than those under positive tilt angles. These findings demonstrate that increasing ambient wind speed reduces flame height, but under identical wind speeds, larger cable tilt angles elevate flame height, exacerbating thermal damage to tunnel ceilings.

3.2.3. Flame Spread Rate

Figure 14 illustrates the flame spread rates of cables under windless and windy conditions. From Figure 14a, it can be observed that the flame spread rate increases with the cable tilt angle, reaching its minimum at a 0° tilt angle. This is because, as the angle increases, the total heat flux in the preheating zone increases, leading to a monotonic increase in the flame spread rate. Specifically, when the cable inclination angle increases, the flame leans closer to the cable surface under the action of buoyancy, increasing the radiative view factor. Meanwhile, the molten cable sheath flows along the inclined direction under the component of gravity, accelerating the forward transfer of heat and thereby shortening the preheating time, which results in an increased spread rate. At a 0° inclination angle, the heat feedback is most dispersed, so the spread rate is the smallest. For example, when the number of cables is three, the flame spread rate exhibits an approximately linear increase with tilt angle, rising by 7.4×10^{-3} cm/s per 10° increment. Additionally, the flame spread rate grows with the number of cables. For example, at a 0° tilt angle, the flame spread rates for single, double, and triple cables are 0.019, 0.022 and 0.032 cm/s, respectively.

Under the influence of ambient wind, the flame spread rate is governed by the competition between two mechanisms: “wind-assisted” and “wind-resistant”. When the flame spread direction is opposite to the wind direction, the wind blows the flame away from the fuel surface, weakening the heat feedback to the preheating zone and thus hindering spread. When the flame spread direction is the same as the wind direction, the flame is pressed toward the unburned area, significantly increasing the heat flux to the preheating zone and accelerating spread. Figure 14b reveals that at a fixed wind speed, the flame spread rate accelerates as the tilt angle shifts from positive to negative. Notably, a significant surge in spread rate occurs at a 10° tilt angle. For instance, at a wind speed of 0.7 m/s, the spread rate at 10° exceeds that at 20° by 0.06 cm/s. This is because at inclination angles of 20° and 30°, the flame spreads upward along the cable, opposite to the ambient wind direction. The wind tilts the flame downstream, causing it to deviate from the cable surface, weakening the heat feedback to the preheating zone and thus suppressing spread. When

the inclination angle decreases to 10°, the flame spread direction becomes consistent with the wind direction. The flame is then pressed toward the unburned cable on the leeward side, enhancing the heat flux to the preheating zone and significantly accelerating the spread rate.

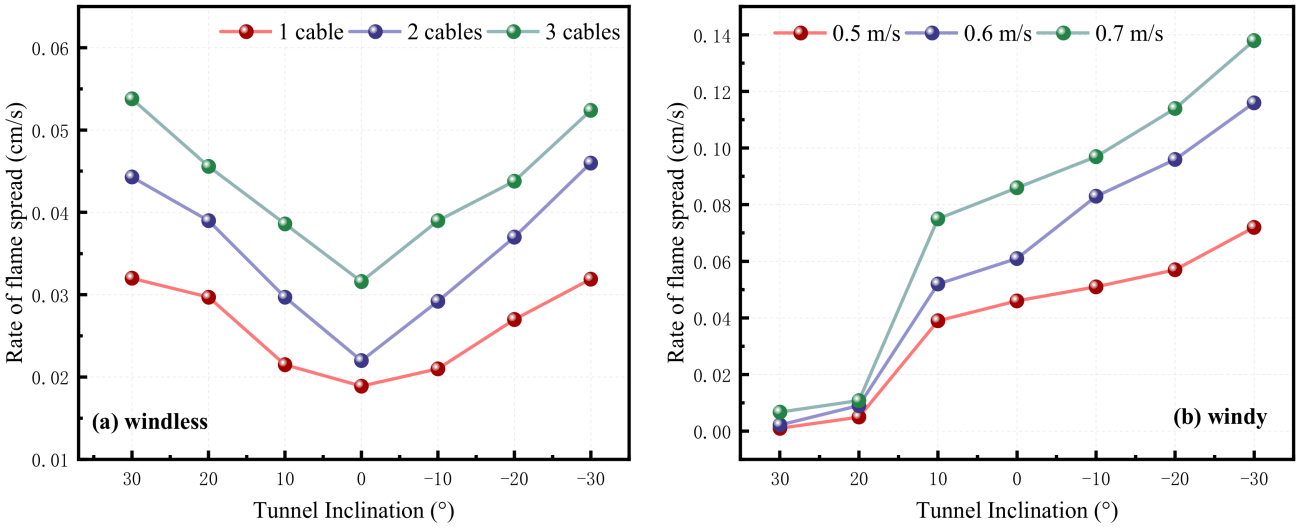


Figure 14. Flame spread rates of cable combustion under windless and ambient wind conditions.

Under a fixed inclination angle, an increase in wind speed intensifies flame tilting, reducing the distance between the flame front and the unburned cable surface and increasing the radiative view factor. Meanwhile, forced convection enhances convective heat transfer from the smoke to the cable surface. The increase in wind speed raises the heat feedback flux from the flame, leading to a monotonic increase in the spread rate. Furthermore, during the transition of the inclination angle from negative to positive, the introduction of wind alters the original buoyancy-dominated evolution pattern, shifting the spread rate curve from a "U-shaped" trend to a "monotonically increasing" trend, reflecting the dominant substitution effect of wind inertial force over buoyancy. Taking an inclination angle of 0° as an example, as the ambient wind speed increases from 0.5 m/s to 0.7 m/s, the flame spread rates of the cable combustion are 0.046 cm/s, 0.061 cm/s, and 0.086 cm/s, respectively. It can be seen that under the action of ambient wind, the flame spread rate of cable combustion changes from an initial trend of first decreasing and then increasing with inclination angle to a trend of gradually increasing.

3.3. Influence of Wind Speed on Fire Zone Temperature and Smoke Behavior

3.3.1. Fire Zone Temperature Variation

Windless conditions

Figure 15 illustrates the temperature evolution in the fire zone under windless conditions. Under windless conditions, the temperature trends at all measuring points are generally consistent: a low peak appears first (during the external heating ignition stage), followed by a gradual increase to the maximum peak, and finally a decay. After the cable is heated, it undergoes pyrolysis and combustion, generating high-temperature smoke, and the temperature near the fire source changes significantly. Upon reaching the combustion stage, the sheath auto-ignites and transfers heat to both ends, melting the sheath and igniting the exposed insulation layer. The smoke and fire plume rise to the tunnel vault, forming an impingement point, and then spread outward. Consequently, the temperatures at the measuring points on both ends of the fire source along the same axis are relatively high.

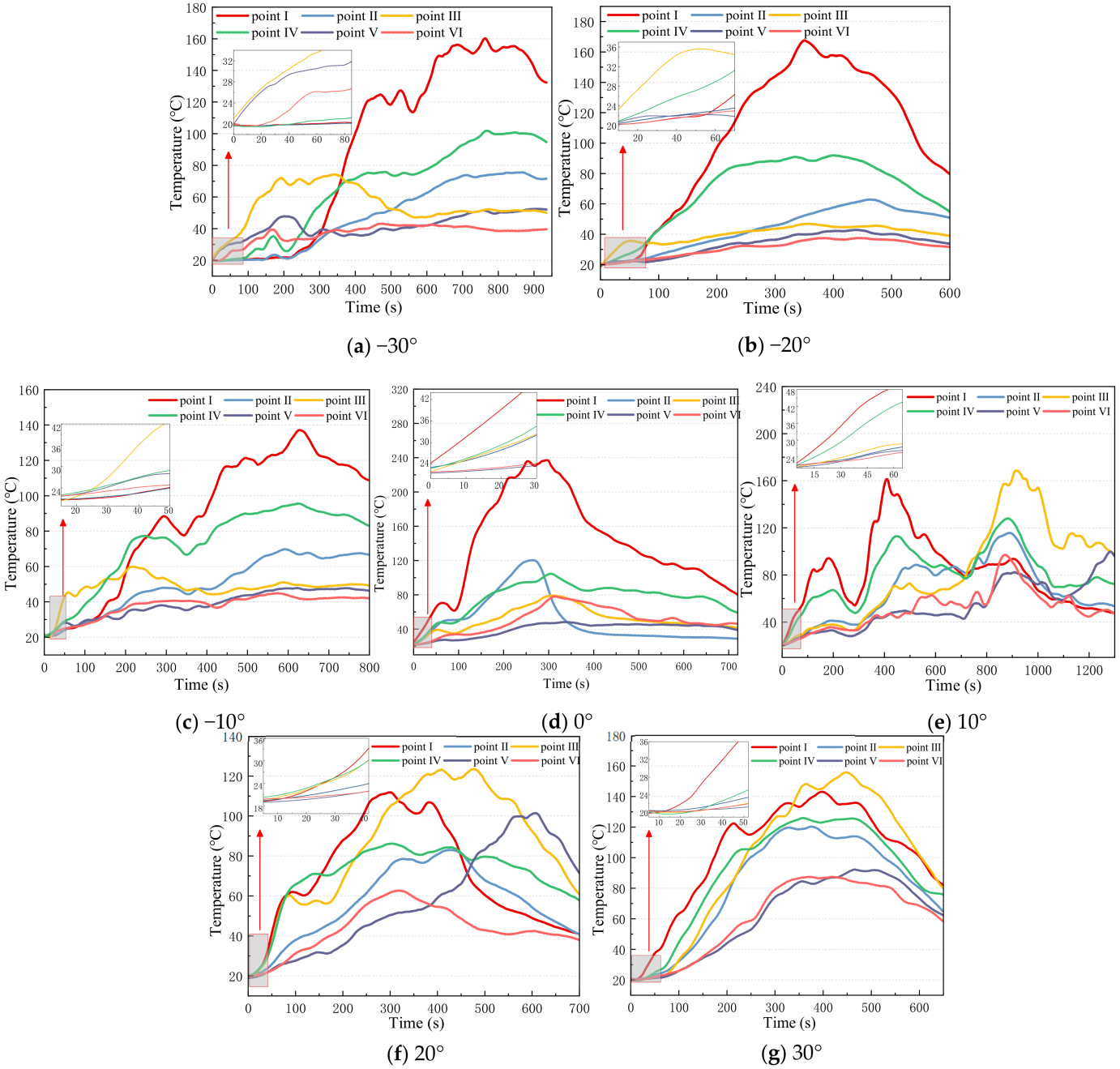


Figure 15. Temperature variation near the fire source in cable combustion under windless conditions.

Monitoring points I and II, III and IV, and V and VI share identical longitudinal positions but are spaced 15 cm apart transversely. Their peak temperatures measure 237, 120.3, 168.5, 128, 101 and 97 °C, respectively. Notably, points V and VI exhibit similar smoke temperature peaks, indicating that off-center fire sources produce smoke temperatures comparable to those along the tunnel's central axis during longitudinal smoke spread.

As the inclination angle changes, the temperature peaks at monitoring points vary significantly. When the tilt angle shifts from negative to positive, the initial temperature rise transitions from point III to point I. This is because the introduction of the inclination angle generates a gravitational component along the tunnel axis, altering the buoyancy-driven smoke flow pattern. As the tunnel inclination angle increases, the axial component of buoyancy intensifies, making the smoke more prone to spreading unidirectionally upward along the ceiling, and the longitudinal temperature distribution exhibits pronounced asymmetry. Specifically, At −30° tilt angle: Point III reaches its peak temperature first (74 °C), followed

by point V (75 °C); At −10° tilt angle: After point III peaks, point IV follows, achieving a maximum of 77 °C. These observations demonstrate that negative tilt angles prioritize smoke migration toward the fire source's right side (e.g., point III), while larger tilt angles amplify longitudinal smoke spread directionality, and smaller tilt angles promote central axis dispersion.

Figure 16 schematically depicts smoke spread patterns under negative tilt angles. Ideally, the smoke would spread first to measurement point III and then to the surrounding measurement points IV and V. Under idealized conditions, smoke initially migrates toward Monitoring Point III, subsequently dispersing to adjacent Points IV and V. As shown in Figure 16a, in a horizontal tunnel (θ = 0°), smoke spreads horizontally from Point III to Point V. When the tunnel is tilted, smoke propagates from Point III to Point V along an upward trajectory inclined at angle θ relative to the horizontal plane. Figure 16b demonstrates that after reaching Point III, smoke ascends toward the tunnel ceiling along the central axis and eventually arrives at Point IV. The chimney effect intensifies with increasing tilt angle θ, amplifying longitudinal smoke spread as the dominant mechanism. Conversely, smaller tilt angles promote smoke dispersion toward the tunnel's central axis, driven by reduced buoyancy-driven momentum. The transition in smoke spread patterns described above is jointly determined by the buoyancy direction and the tunnel geometry. In a horizontal tunnel (θ = 0°), buoyancy acts vertically upward. After the smoke impinges on the ceiling, it forms a radially symmetric jet that spreads outward in all directions centered directly above the fire source. When the tunnel has an inclination angle θ, buoyancy generates an axial component $g \cdot \sin\theta$ along the tunnel, which drives the smoke to preferentially spread upward along the longitudinal direction. According to the theory of smoke flow in inclined enclosures, when the axial component of buoyancy exceeds the inertial force threshold, the smoke transitions from a lateral diffusion mode to a longitudinal spread mode [38].

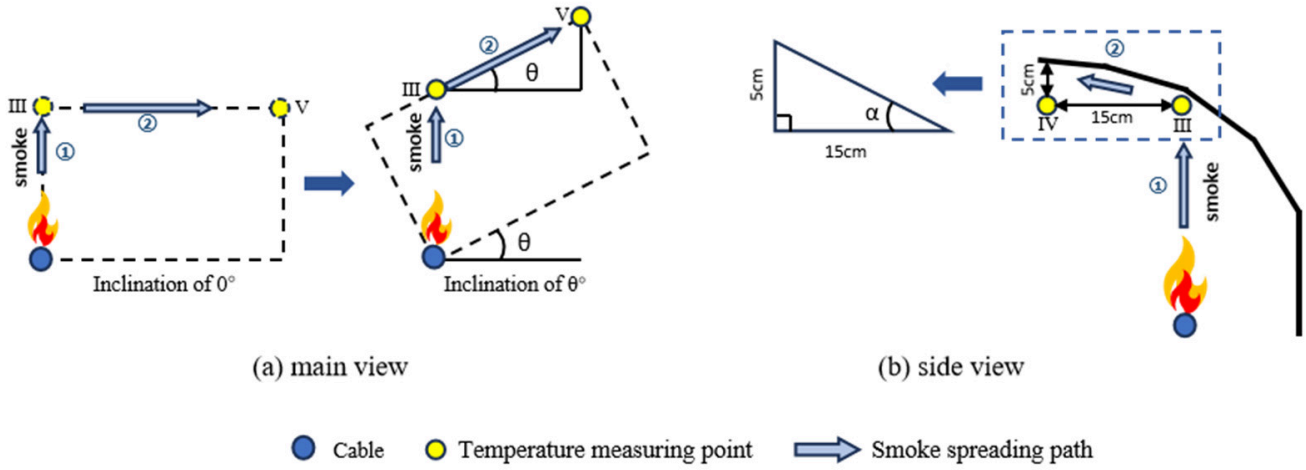


Figure 16. Schematic diagram of smoke spread under negative tilt angles.

Data from Figure 15 further elucidate this behavior. At θ = 20°, smoke primarily diffuses toward the central axis, with the temperature at Point IV rising after Point III. This suggests that lateral dispersion competes with longitudinal spread under moderate tilt conditions. However, at θ = 30°, longitudinal spread becomes dominant, as evidenced by the delayed temperature rise at Point V following Point III. These observations imply a critical tilt angle threshold between 20° and 30°, where the balance between buoyancy forces (enhanced by the chimney effect) and inertial forces (governing lateral dispersion) shifts abruptly.

The transition in spread direction is mechanistically attributed to the dual role of tilt angle in modifying both the effective buoyancy head and the geometric constraints of the tunnel. Larger tilt angles ($\theta > 20°$) amplify the chimney effect by increasing the vertical height difference between fire source and ceiling, thereby strengthening upward thermal acceleration. Simultaneously, the inclined tunnel geometry restricts lateral smoke entrainment, forcing longitudinal flow. In contrast, smaller tilt angles ($\theta < 20°$) weaken buoyancy dominance, allowing turbulent mixing and pressure gradients to redirect smoke toward the central axis. This nonlinear interplay highlights the sensitivity of smoke dynamics to minor geometric variations, with profound implications for fire detection system placement and emergency ventilation strategies in inclined tunnels.

Windy conditions

To investigate the influence of varying ambient wind speeds on temperature changes in smoke near the fire source, this study focuses on monitoring points exhibiting significant thermal fluctuations. Figure 17 presents the temperature variations at selected monitoring points under a wind speed of 0.5 m/s and a 0° tilt angle.

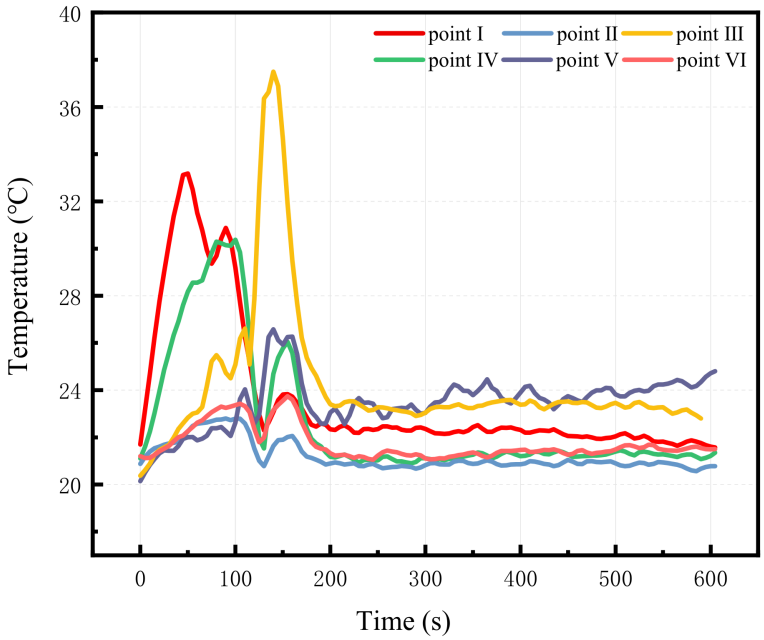


Figure 17. Temperature variation near the fire source under 0.5 m/s wind speed and 0° tilt angle.

As shown in the figure, compared to smoke temperatures under windless conditions, the introduction of 0.5 m/s wind speed drastically reduces smoke temperatures. For instance, the maximum temperature at Monitoring Point III drops from 168 °C (windless) to 37.85 °C (windy). This demonstrates that ambient wind significantly suppresses smoke temperatures near the fire source, with Point III exhibiting the highest residual temperature and most pronounced thermal variations among all monitoring points. The prominence of Point III's temperature response stems from its strategic positioning within the flame plume's primary upward trajectory. Under windless conditions, buoyancy-dominated flow directs high-temperature smoke vertically toward this point. However, wind-induced tilting of the flame plume redistributes heat, yet Point III remains within the residual thermal core, capturing the most representative temperature dynamics. This positional sensitivity underscores its utility as a key indicator for evaluating wind effects on fire thermal behavior. Therefore, data from Point III are selected for detailed analysis of temperature evolution under varying wind speeds.

As shown in Figure 18, the smoke temperature gradually decreases with increasing ambient wind speed. For instance, at a tilt angle of 10°, when the wind speed rises from 0.5 m/s to 0.7 m/s, the temperature drops from 45 °C to 28 °C. Additionally, distinct temperature trends are observed across different tilt angles. At tilt angles of −30° and −20°, the smoke temperature initially rises gradually, stabilizes, and then declines, with the entire combustion process completing within 120 s. For tilt angles of −10°, 0°, and 10°, the temperature rapidly increases to a peak before sharply dropping to ambient levels within 200 s. At tilt angles of 20° and 30°, the temperature rises slowly at first, then decreases with fluctuations after reaching stability, with a maximum temperature of only 32 °C.

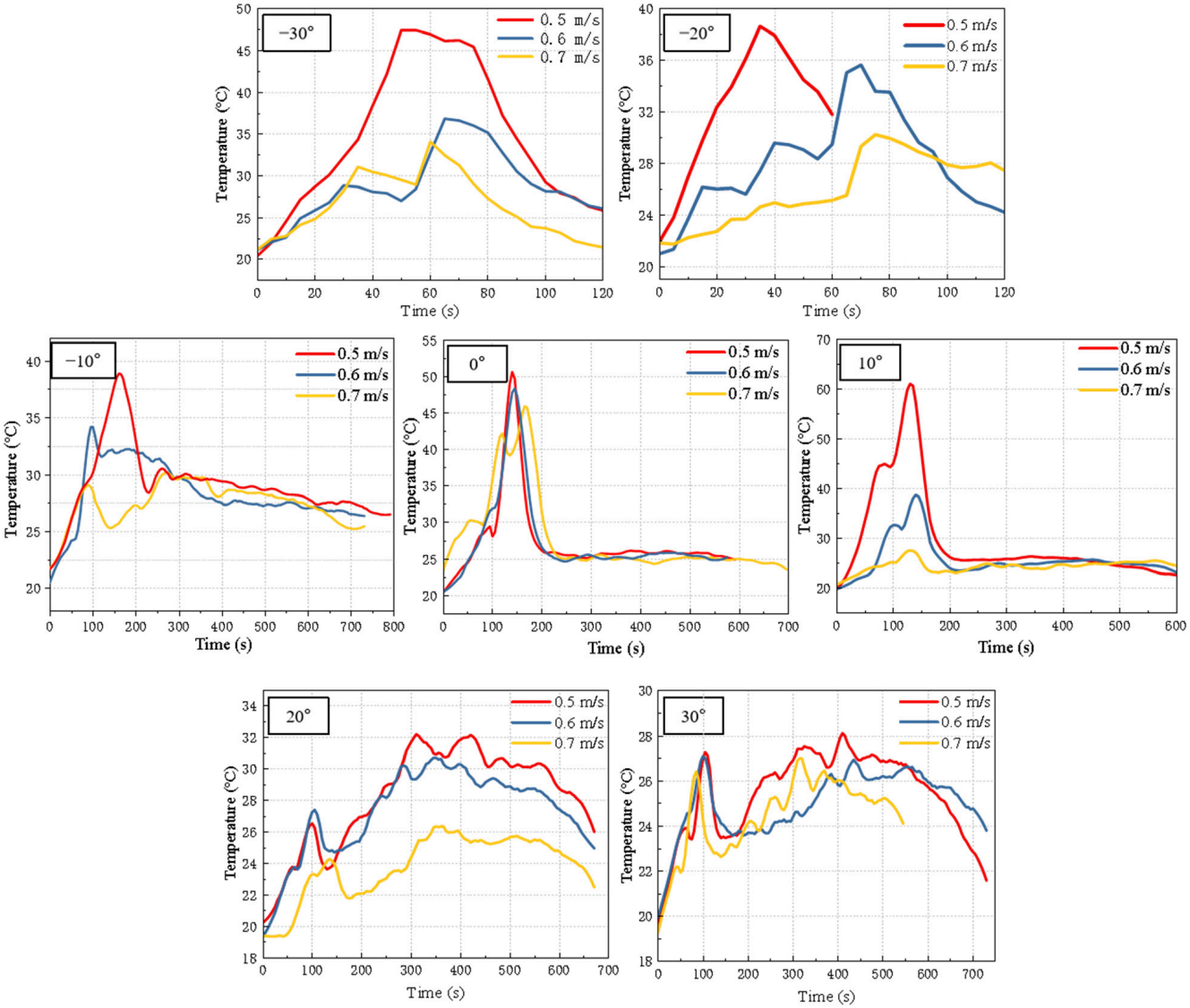


Figure 18. Temperature variation near the fire source during cable combustion under windy conditions.

The ambient wind accelerates the entrainment of cold air into the smoke plume, significantly reducing temperatures. However, the interaction between wind and tilt angle introduces complex dynamics. At negative tilt angles: −30° and −20°, although the increased tilt angle promotes flame spread, the opposing effect of wind suppresses combustion. This results in an initial temperature rise followed by rapid decay to ambient levels within 120 s. For tilt angles of −10°, 0°, and 10°, wind-enhanced smoke entrainment accelerates post-peak temperature decline. Conversely, at positive tilt angles: 20° and 30°, wind

and tilt synergistically intensify flame spread and combustion, while smoke entrainment simultaneously causes a slow, fluctuating temperature decrease after peaking.

Based on the above analysis, the trend in flue gas temperature undergoes a significant shift at inclination angles of -20° and 20°, indicating that these two angles can be regarded as critical points for the temperature change trend. When the inclination angle exceeds or falls below this critical range, the trend in flue gas temperature will vary differently with changes in inclination angle.

3.3.2. A Critical State Theory Model Based on the Richardson Number

To characterize the transition between wind-dominated and buoyancy-dominated behaviors, a modified Richardson number (Ri^*) is introduced. In general, Richardson-number-type parameters are used to describe the relative importance of buoyancy and inertial effects [39]. In the present inclined tunnel fire scenario, Ri^* is defined to represent the competition between buoyancy/slope-induced stack effects and longitudinal wind inertia.

The formulation of Ri^* for the present inclined tunnel fire scenario is developed under the following assumptions. The smoke flow during the stable combustion stage is regarded as quasi-steady, and the density difference between hot smoke and ambient air is assumed to be primarily induced by temperature rise. Pressure variation is neglected, allowing the ideal gas relationship to be used for estimating the density ratio. In the inclined tunnel, the stack effect is represented by the axial component of buoyancy along the tunnel direction, while the measured longitudinal wind speed is used to characterize the wind-induced inertial effect.

Accordingly, the numerator of Ri^* represents the buoyancy-related driving effect, whereas the denominator represents the wind-induced inertial effect. Therefore, a smaller Ri^* indicates that flame deflection and smoke transport are mainly controlled by longitudinal ventilation, whereas a larger Ri^* indicates that buoyancy and slope-induced stack effects become dominant. The expression is derived as follows:

$$Ri = \frac{\partial \rho / \partial z}{(\partial u / \partial z)^2} \frac{g}{\rho} \tag{11}$$

In fire plume or tunnel smoke flow, simplified forms are commonly used:

$$Ri = \frac{g \cdot \Delta\rho/\rho \cdot L}{u^2} = \frac{g' \cdot L}{u^2} \tag{12}$$

where g is the gravitational acceleration (9.81 m/s^2); $g' = g\Delta\rho/\rho$ is the reduced gravitational acceleration; $\Delta\rho$ is the density difference; L is the characteristic length, taken as the tunnel height of 0.4 m; u is the ambient velocity.

In fire smoke, the density difference is primarily caused by temperature differences. Based on the ideal gas equation of state $\rho \propto 1/T$ and assuming negligible pressure changes, we obtain:

$$\frac{\Delta\rho}{\rho_\infty} \approx \frac{\Delta T}{T_\infty} \tag{13}$$

Among these, $\Delta T = T - T_\infty$ represents the characteristic temperature rise during the stable combustion phase above the fire source, calculated as the difference between the peak temperature at measurement point III and the ambient temperature; T_∞ is the absolute ambient temperature. According to actual measurements during the experiment, the ambient temperature was stable at 20 °C. Therefore:

$$g' = g\frac{\Delta\rho}{\rho_\infty} \approx g\frac{\Delta T}{T_\infty} \tag{14}$$

In an inclined tunnel, the driving force of the stack effect originates from the axial component of buoyancy along the tunnel. The buoyancy-driven acceleration along the tunnel axis is $g \cdot \sin|\theta|$. Substituting the above parameters yields the modified Richardson number Ri^*:

$$Ri^* = \frac{g \cdot \sin|\theta| \cdot (\Delta T / T_\infty) \cdot L}{u^2} \quad (15)$$

where θ represents the tunnel inclination angle, expressed as an absolute value. Since Ri^* represents the relative strength of buoyancy and wind-induced inertia, $Ri^* \approx 1$ indicates that the two mechanisms are of comparable importance. In practical fire experiments, however, the transition between the two regimes does not occur at a single sharp value because of flame fluctuation, turbulent mixing, and measurement uncertainty. Therefore, a transition interval of $0.5 \leq Ri^* \leq 2$ is adopted around the theoretical balance point of $Ri^* \approx 1$. This interval can be regarded as an order-of-magnitude buffer zone, within which neither buoyancy nor wind-induced inertia can be considered independently dominant. Accordingly, $Ri^* < 0.5$, $0.5 \leq Ri^* \leq 2$, and $Ri^* > 2$ were adopted in this study to identify wind-dominated, transition, and buoyancy-dominated regimes, respectively.

Using experimental data at wind speed u = 0.5 m/s, substitute the corresponding ΔT values for each tilt angle into Equation (15) to calculate the Ri^* values. The results are shown in Table 4.

Table 4. Calculation of richardson number Ri^* values at different inclination angles.

θ/°	−30	−20	−10	0	10	20	30
ΔT/K	96	45	13.6	17	25	49	85
Sin	0.5	0.342	0.17	0	0.173	0.34	0.5
Ri^*	2.57	0.82	0.12	0	0.23	0.89	2.27

The experimental observations further support this classification. When $|\theta| = 20°$, Ri^* values of 0.82 and 0.89 were obtained, both of which fall within the transition interval of $0.5 \leq Ri^* \leq 2$. This indicates that buoyancy and wind-induced inertia are of comparable importance within this inclination range, providing theoretical support for identifying $|\theta| \approx 20°$ as a transition region.

When $Ri^* < 0.5$, flame deflection and smoke transport are mainly controlled by longitudinal ventilation. When $0.5 \leq Ri^* \leq 2$, mixed-control behavior is observed. When $Ri^* > 2$, the slope-induced stack effect becomes increasingly significant, and buoyancy-driven smoke movement dominates. Therefore, the proposed Ri^*-based classification provides a practical engineering criterion for identifying dominant fire behavior regimes in inclined tunnel cable fires under the tested conditions.

3.3.3. Smoke Variation in Fire Zones

CO gas release

Figure 19 depicts the variations in CO gas release under different ambient wind speeds. As shown in Figure 19, the CO release rate exhibits a similar trend across all conditions, increasing approximately linearly with time until the cable combustion enters the decay phase, after which the release rate gradually slows. Under varying wind speeds, the CO release rate decreases as the wind speed increases. For example, at a tilt angle of 30°, raising the wind speed from 0.5 to 0.7 m/s reduces the average release rate from 0.63 to 0.53 ppm/s.

The phenomenon that the CO release rate decreases with increasing wind speed can be explained by two mechanisms: flue gas dilution and changes in combustion efficiency. First, an increase in ambient wind speed significantly enhances air entrainment and mixing within the tunnel, rapidly diluting the CO in the fire smoke, thereby reducing the CO mass flux

passing through the measurement cross-section per unit time and lowering the measured concentration. Second, the effect of wind speed on the cable combustion process is twofold: in the low-to-moderate wind speed range (0.5~0.7 m/s), the increased oxygen supply to the fire zone promotes more complete combustion of volatile combustibles, relatively reducing the generation rate of the incomplete combustion product CO. Meanwhile, the cooling effect of the airflow on the flame front does not yet dominate, and the overall combustion efficiency improves. Consequently, CO release decreases with increasing wind speed. This trend remains valid even under a large inclination angle (e.g., 30°), indicating that within this wind speed range, the dilution and combustion-enhancing effects jointly dominate, while the promoting effect of wind-induced flame deflection on CO generation is not yet significant.

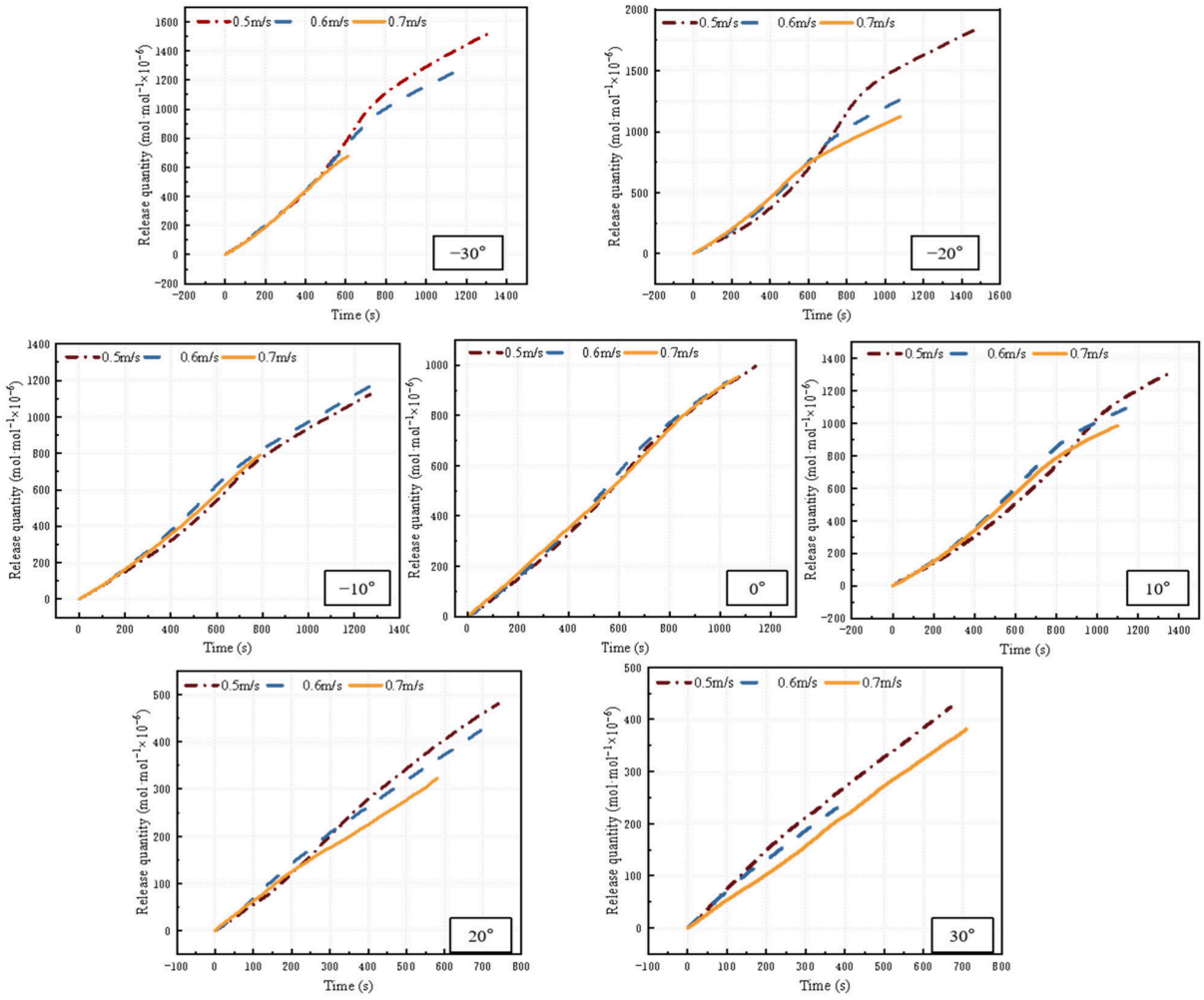


Figure 19. CO gas release under varying ambient wind speeds.

Furthermore, at a wind speed of 0.5 m/s, the CO concentrations at tilt angles of −30° and −20° are relatively close, measuring 424 ppm and 480 ppm, respectively. Similarly, at tilt angles of −10°, 0°, and 10°, the CO concentrations are 1304.5 ppm, 995 ppm, and 1117 ppm, while at tilt angles of 20° and 30°, the values reach 1828 ppm and 1521 ppm.

According to the criterion based on the modified Richardson number: when $|\theta| < 20°$, forced convection dominates. Ambient wind exerts strong dilution and transport effects on the smoke, while the ample oxygen supply promotes relatively complete combustion, resulting in a low CO generation rate. Consequently, the CO concentration at the measuring point remains in a low range. When $10° < |\theta| < 20°$, buoyancy and inertial forces compete, and the flow field exhibits an unstable transitional regime. In this range, enhanced turbulent entrainment intensifies local oxygen concentration fluctuations, leading

to unstable combustion efficiency and an increased CO generation rate. Meanwhile, the prolonged residence time of smoke in the tunnel weakens the dilution effect, causing a significant increase in the accumulated CO concentration. When $|\theta| > 20°$, the stack effect completely dominates. The flame leans closer to the cable surface at larger inclination angles, enhancing radiative heat feedback and greatly increasing the cable pyrolysis rate. Although ambient wind still exerts some dilution, the CO generation rate per unit time far exceeds the dilution capacity. Furthermore, beyond 20°, the flame spread direction opposes the wind direction (wind-blocking mechanism). The flame is blown away from the fuel surface, exacerbating incomplete combustion and further elevating CO yield. The above variation pattern is in excellent agreement with the critical angle of flow regime transition determined by the Richardson number, confirming the physical universality of this critical angle in the evolution of smoke composition.

CO_2 gas release

As shown in Figure 20, the CO_2 release rate decreases with increasing wind speed. Its physical mechanism is similar to that of CO, mainly attributable to the dilution effect of ambient wind and changes in combustion efficiency. The increase in wind speed enhances air entrainment and turbulent mixing within the tunnel, leading to rapid dilution of the CO_2 concentration in the smoke. Moreover, the trend of CO_2 gas release is generally consistent under different conditions, increasing approximately linearly with time.

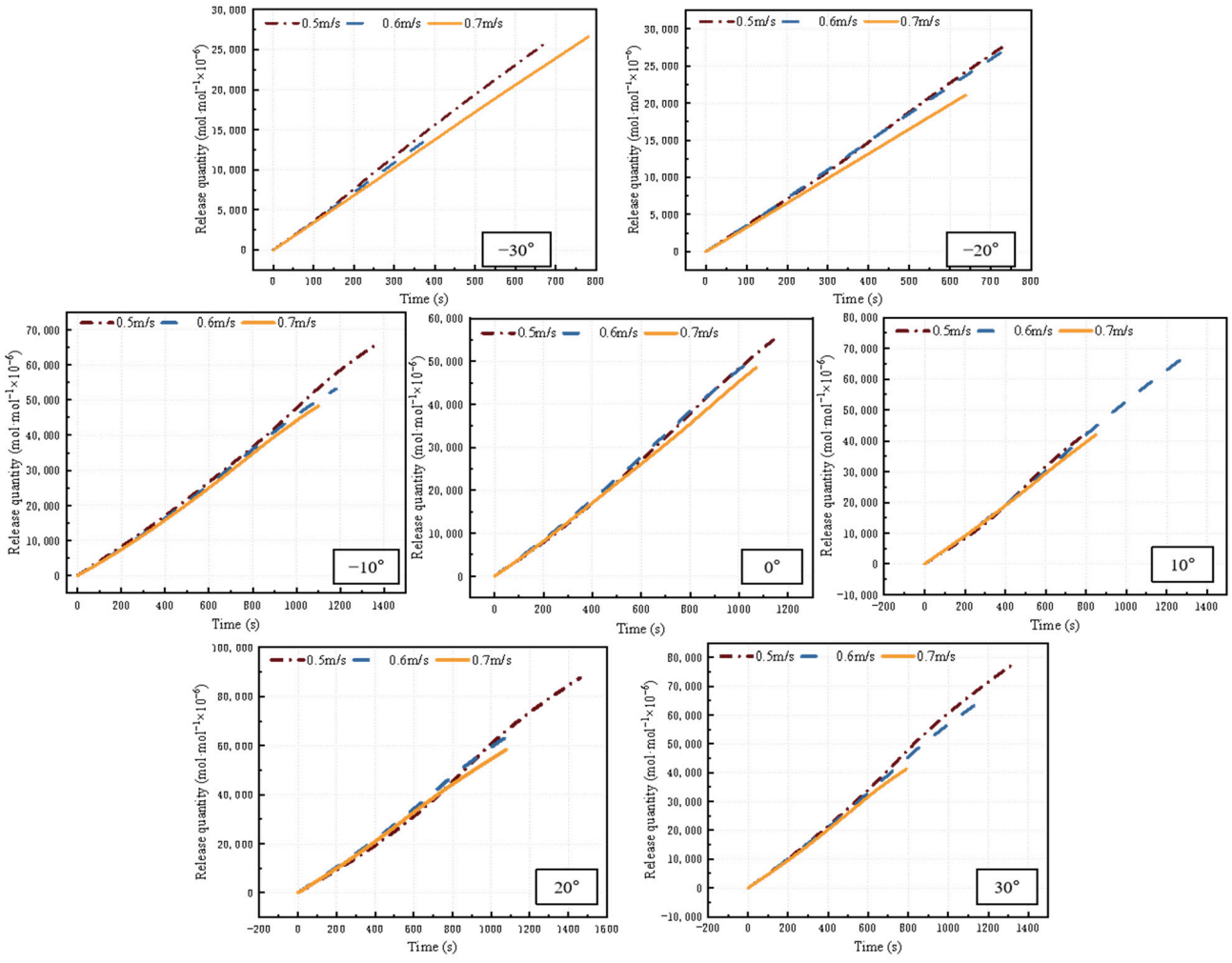


Figure 20. CO_2 gas release under varying ambient wind speeds.

For example, at a tilt angle of 10°, when the wind speed rises from 0.5 to 0.7 m/s, the CO_2 release rate increases by approximately 48, 44 and 43 ppm/s, respectively. At a wind speed of 0.5 m/s, when the tilt angles of −30° and −20°: CO_2 concentrations are 2.56% and 2.8%, respectively; when the tilt angles of −10°, 0°, and 10°: CO_2 concentrations measure 6.52%, 5.5%, and 4.24%; when the tilt angles of 20° and 30°: CO_2 concentrations reach 8.76% and 7.7%. These results further validate that tilt angles of −20° and 20° act as critical thresholds for gas concentration dynamics.

Below −20°, limited oxygen availability restricts combustion efficiency, leading to lower CO_2 emissions. Between −20° and 20°, enhanced turbulence and heat feedback optimize combustion, maximizing CO_2 production. Beyond 20°, despite stronger wind-driven dilution, intensified thermal decomposition of cable materials elevates CO_2 release, though at a reduced rate due to accelerated heat dissipation.

4. Conclusions

This study experimentally analyzed the combustion characteristics of cables using a synchronous thermal analyzer and a cone calorimeter to determine their fundamental combustion parameters. A scaled inclined tunnel cable fire test platform was constructed based on similarity principles, and combustion experiments were conducted under varying ambient wind speeds. The main conclusions are as follows:

(1) The ignition time of the cable gradually shortens as the applied heat radiation intensity increases. When the heat radiation intensity reaches 50 kW/m^2, the cable ignition time shortens to 16 s, and the ignition temperature of the cable is determined to be 295.1 °C. The heating process of the cable conforms to the ignition model for thermally medium materials. As thermal radiation intensity increases, the peak heat release rate of the cable exhibits an increasing trend, indicating heightened fire hazard potential.

(2) In the absence of ambient airflow, the tunnel inclination modulates buoyancy direction and stack effect intensity, exerting a non-monotonic influence on flame morphology, height, and propagation rate. The smoke propagation path gradually shifts from centerline-dominated diffusion to longitudinal-dominated spread as the inclination angle increases.

(3) Quantitative analysis using the modified Richardson number (*Ri**) demonstrates that wind-driven flow dominates across the experimental wind speed range. Inclination angles of −20° and 20° represent critical thresholds for rapid versus gradual temperature changes. In ventilation design, heightened attention must be given to the small positive inclination range (e.g., 10°) due to the potential unexpected high risk from "wind-assisted preheating." For tunnels with greater inclinations (>20°), emphasis should be placed on enhancing smoke control and detection in the uphill direction.

(4) Both CO and CO_2 release rates decrease with increasing wind speeds but exhibit an approximately linear rise over time. The gas concentration trends further validate that tilt angles of −20° and 20° serve as critical thresholds for the trend of fast and slow changes in gas concentration.

It should be noted that this study focused on one representative flame-retardant PVC cable type, namely ZR-RVV cable. Therefore, the obtained combustion characteristics, flame-deflection behavior, and ventilation-related implications are most directly applicable to tunnel scenarios where similar flame-retardant PVC cables are used. Since cable structure, insulation material, sheath composition, and flame-retardant additives may affect ignition, heat release, and flame spread behavior, further studies involving different cable types are needed before the proposed correlations and ventilation implications can be generalized to all tunnel cable systems.

Author Contributions: Conceptualization, L.W.; Methodology, L.W. and R.L.; Validation, Q.G.; Formal Analysis, Y.Z. (Yutao Zhang); Data curation, L.W. and R.L.; Investigation, J.B.; Writing—original draft, Y.Z. (Yutao Zhang) and L.W.; Writing—review and editing, Y.Z. (Yutao Zhang), L.W. and R.L.; Visualization, H.L.; Supervision, H.S.; Funding acquisition, Y.Z. (Yutao Zhang) and Y.Z. (Yuanbo Zhang). All authors have read and agreed to the published version of the manuscript.

Funding: This work was supported by the National Natural Science Foundation of China (No. 52574273), Postdoctoral Fellowship Program (Grade C) of CPSF, China (No. GZC20232138), Shaanxi Provincial Outstanding Youth Science Foundation Program (No. 2025JC-JCQN-024).

Data Availability Statement: The original contributions presented in this study are included in the article. Further inquiries can be directed to the corresponding author.

Conflicts of Interest: The authors declare no conflicts of interest. The company affiliation had no role in the design of the study, data collection, analysis, interpretation of data, writing of the manuscript, or decision to publish the results.

References

1. Yuan, D.; Zhang, G.; Lin, C.; Lv, H.; Zhang, K.; Lin, F.; Gu, H. Fast elimination of cable fire smoke in underground tunnels using acoustic agglomeration technology. *Tunn. Undergr. Space Technol.* **2021**, *117*, 104154. [CrossRef]
2. Cheng, X.; Li, D.; Li, H.; Peng, X.; Zhao, L.; Zhao, W. Stability analysis of a 3D shallow tunnel face considering the inclined excavation and inclined ground surface. *Comput. Geotech.* **2024**, *165*, 105915. [CrossRef]
3. Shao, Z.; Bi, M.; Cong, H.; Bi, H.; Ye, Y.; Liu, J. Experimental study on ceiling maximum temperature and back-layering length in inclined tunnel fires. *Int. J. Heat Mass Transf.* **2025**, *239*, 126621. [CrossRef]
4. Wang, J.; Huang, D.; Song, Y.; Lu, K. Improved prediction model for ceiling maximum smoke temperature in the uphill tunnel fires using water spray system. *Case Stud. Therm. Eng.* **2025**, *66*, 105739. [CrossRef]
5. Sun, C.; Weng, M.; Liu, F.; Zhang, Y.; Zhang, X. Investigating the influence of stack effect on plume inclination and maximum ceiling temperature position in inclined tunnel fires. *Int. Commun. Heat Mass Transf.* **2024**, *159*, 108290. [CrossRef]
6. Gao, Z.; Li, L.; Sun, C.; Zhong, W.; Yan, C. Effect of longitudinal slope on the smoke propagation and ceiling temperature characterization in sloping tunnel fires under natural ventilation. *Tunn. Undergr. Space Technol.* **2022**, *123*, 104396. [CrossRef]
7. Bai, Z.P. Burning characteristics of power cables with cone calorimeter. *Heliyon* **2024**, *10*, e25103. [CrossRef] [PubMed]
8. Wang, Z.; Wang, J. An experimental study on the fire characteristics of new and aged building wires using a cone calorimeter. *J. Therm. Anal. Calorim.* **2019**, *135*, 3115–3122. [CrossRef]
9. Wang, Z.; Wang, J. Comparative thermal decomposition characteristics and fire behaviors of commercial cables. *J. Therm. Anal. Calorim.* **2021**, *144*, 1209–1218. [CrossRef]
10. Shi, Q.; Song, W.; Jia, B.; Wang, B.; Zuo, J. Experimental analysis of nuclear grade cable based on fire combustion characteristics and pyrolysis behavior. *Nucl. Sci. Eng.* **2024**, *44*, 880–885. (In Chinese)
11. Wang, Z.; He, H.; Zhu, J.; Huang, D. Analysis of smoke generation characteristics and smoke toxicity of commonly utilized cables under fire conditions. *Saf. Environ. Eng.* **2023**, *30*, 17–22+54. [CrossRef]
12. Guo, J.; Gao, W.; Cai, G.; Wen, H. Experimental study on combustion characteristics and hazard of the flame-retardant cables in urban utility tunnel. *Chin. J. Undergr. Space Eng.* **2023**, *19*, 1009–1018. (In Chinese)
13. Chen, C.; Du, W.; Xu, T. Experimental study on combustion behavior of U-shaped cables with different bending forms and angles. *Fire* **2023**, *6*, 348. [CrossRef]
14. Peng, L.; Huang, X.; Wang, J.; Zhu, H. Influence mechanism of temperature field inside the cable on dynamic process of cable pyrolysis. *Fire Saf. J.* **2023**, *141*, 103972. [CrossRef]
15. Zheng, X.; Cai, G.; Guo, J.; Gao, W.; Huang, Y.; Tong, X. Combustion characteristics and thermal decomposition mechanism of the flame-retardant cable in urban utility tunnel. *Case Stud. Therm. Eng.* **2023**, *44*, 102887. [CrossRef]
16. Huang, P.; Lin, X.; Liu, C.; Zeng, F.; Lin, K.; Yang, M.; Yu, L. Experimental study on the smoke temperature distribution of cable tray fires of utility tunnel under different entrainment restriction conditions. *J. Saf. Environ.* **2024**, *24*, 897–906. [CrossRef]
17. Chen, C.; Zuo, B.; Xu, T.; Jiao, W. Comparative study on combustion temperature distribution of inclined cables under open condition and with cable trough. *J. Cent. South Univ. (Sci. Technol.)* **2023**, *54*, 3205–3212. [CrossRef]
18. Chen, C.; Xu, T.; Chen, J.; Zuo, B. Combustion characteristics of trays cable in different layouts. *J. Cent. South Univ. (Sci. Technol.)* **2022**, *53*, 4326–4334. [CrossRef]
19. Xing, C.; Hung, X.; Zhu, H.; Huang, M.; Deng, H.; Amokrane, A.; Li, L.; Yang, P. Thermal radiation from a moving cable fire along the cable tray in a full-size corridor. *Fire Technol.* **2024**, *61*, 2265–2283. [CrossRef]

20. Xu, D.; Li, Y.; Li, J.; Zhong, H.; Li, J.; Tu, D.; Huang, Y. Evaluating the combustion and flame extension characteristics of cable fire in utility tunnels with spontaneous combustion scenarios: An experimental study. *Tunn. Undergr. Space Technol.* **2023**, *140*, 105244. [CrossRef]
21. Viitanen, A.; Hostikka, S.; Vaari, J. CFD simulations of fire propagation in horizontal cable trays using a pyrolysis model with stochastically determined geometry. *Fire Technol.* **2022**, *58*, 3039–3065. [CrossRef]
22. Hay, W.; Seguillon, L.; Boyer, G. Numerical simulations of a PVC cable fire on long cable-trays in a mechanically ventilated large scale facility. *Fire Saf. J.* **2023**, *138*, 103799. [CrossRef]
23. Liu, S.; Liu, J.; Ying, D.; Hu, L.; Ming, X. Study on the Smoke Characteristics of a Cable Fire in an L-Shaped Utility Tunnel under Different Ventilation Conditions. *J. Pipeline Syst. Eng. Pract.* **2024**, *16*, 04024070. [CrossRef]
24. Zhu, X.; Wu, J.; Bai, Y.; Wang, D.; Zhang, J. Integrating FBN and FDS for quantitative risk assessment of cable fire in utility tunnel. *J. Loss Prev. Process Ind.* **2024**, *88*, 105266. [CrossRef]
25. Tyas, D.; Bagshaw, D.; Plummer, J.; Nyogeri, L. Modelling the heat release rate of PRISME experimental cable fires in a confined, ventilation controlled, environment using FLASH-CAT and FDS. *Fire Saf. J.* **2023**, *139*, 103828. [CrossRef]
26. Prétrel, H.; Zavaleta, P.; Suard, S. Experimental study on the effect of mechanical ventilation on cable tray fires in compartments. *Fire Saf. J.* **2023**, *138*, 103792. [CrossRef]
27. Bai, Z.; Yu, Y.; Lv, K.; Lv, H.; Yao, H.; Yang, C. Experimental study on influence of natural ventilation on near wall fire in cable tunnel. *Eng. Lett.* **2023**, *31*, 689–694. Available online: https://www.engineeringletters.com/issues_v31/issue_2/EL_31_2_25.pdf (accessed on 30 June 2026).
28. Xu, D.; Li, Y.; Li, J.; Zhong, H.; Li, J.; Huang, Y. Combustion characteristics and flame morphological evolution of double-layer cable fires in urban utility tunnels with various laying spacings. *Energy* **2025**, *315*, 134324. [CrossRef]
29. Zhang, Y.; Guo, Q.; Zhang, Y.; Deng, J.; Li, Y.; Li, H. Study on transformation characteristics and oxidation kinetics of coal spontaneous combustion induced by thermal radiation. *Therm. Sci. Eng. Prog.* **2025**, *64*, 103767. [CrossRef]
30. Ingason, H.; Li, Y.Z.; Lönnermark, A. Model scale tunnel fire tests with longitudinal ventilation. *Fire Saf. J.* **2010**, *45*, 371–384. [CrossRef]
31. Zimny, M.; Antosiewicz, P.; Krajewski, G.; Węgrzyński, W. Several problems with Froude-number based scale modeling of fires in small compartments. *Energies* **2019**, *12*, 3625. [CrossRef]
32. *JTG/T D70/2-02-2014*; Guidelines for Design of Ventilation of Highway Tunnels. China Communications Press: Beijing, China, 2014. Available online: https://www.doc88.com/p-6941781652395.html (accessed on 30 June 2026).
33. *JTG/T D70/2-01-2014*; Guidelines for Design of Lighting of Highway Tunnels. China Communications Press: Beijing, China, 2014. Available online: http://www.weboos.cn/assets/basicStandard/std_535187.pdf (accessed on 30 June 2026).
34. Xu, L.; Zhang, H.; Wan, Y. Study on Ignition of Thermoplastic Linings. *Eng. Sci.* **2007**, *9*, 39–43. (In Chinese) [CrossRef]
35. Kurioka, H.; Oka, Y.; Satoh, H.; Sugawa, O. Fire properties in near field of square fire source with longitudinal ventilation in tunnels. *Fire Saf. J.* **2003**, *38*, 319–340. [CrossRef]
36. Chen, Y.; Zhao, Y.; Zhong, T.; Zhao, H.; Zhao, Q.; Zhang, Y. Experimental analysis and theoretical prediction model of flame tilt angle in longitudinally ventilated inclined tunnel fires. *Fire Technol.* **2025**, *62*, 55. [CrossRef]
37. Qiu, M.; Li, Y.; Xu, L.; Zhao, S.; Li, L.; Zhong, H. Experimental study on flame behaviour characteristics induced by unequal double fires in a tunnel under different ventilation modes. *Tunn. Undergr. Space Technol.* **2025**, *163*, 106730. [CrossRef]
38. Kunsch, J. Simple model for control of fire gases in a ventilated tunnel. *Fire Saf. J.* **2002**, *37*, 67–81. [CrossRef]
39. Yin, L.; Xing, Z.; Zhu, F.; Xu, H.; Wu, J.; Cheng, Y. Numerical simulation study of gas leakage in underground utility tunnel. *J. Saf. Sci. Technol.* **2024**, *20*, 99–104. (In Chinese) [CrossRef]

Disclaimer/Publisher's Note: The statements, opinions and data contained in all publications are solely those of the individual author(s) and contributor(s) and not of MDPI and/or the editor(s). MDPI and/or the editor(s) disclaim responsibility for any injury to people or property resulting from any ideas, methods, instructions or products referred to in the content.